Diverse Approaches to Ultralight Dark Matter

by

Thomas Bouley

A dissertation accepted and approved in partial fulfillment of the
requirements for the degree of
Doctor of Philosophy
in Physics

Dissertation Committee:
Graham Kribs, Chair
Tien-Tien Yu, Advisor
Raymond Frey, Core Member
David Allcock, Core Member
Daniel Dugger, Institutional Representative

University of Oregon
Spring 2025

© 2025 Thomas Bouley
This work is openly licensed via CC BY 4.0

DISSERTATION ABSTRACT

Thomas Bouley

Doctor of Philosophy in Physics

Title: Diverse Approaches to Ultralight Dark Matter

The composition of most of the matter in the universe remains unknown. This matter, known as dark matter, is inferred to exist only through its gravitational interactions with ordinary matter, as observed in cosmology and astrophysics. Many hypotheses have been proposed regarding the composition of dark matter. One class of candidates, known as ultralight dark matter (ULDM), is light enough that its de Broglie wavelength is macroscopically large. In this work, we examine three distinct approaches to searching for ultralight dark matter.

First, we investigate the effects of quadratically coupled ultralight dark matter on the predictions of Big Bang Nucleosynthesis (BBN) The presence of ultralight dark matter can modify the effective values of fundamental constants during Big Bang Nucleosynthesis, modifying the predicted abundances of the primordial elements such as Helium-4. We improve upon the existing literature in two ways: firstly, we take into account the thermal mass acquired by the ultralight dark matter due to its quadratic interactions with the Standard Model bath, which affects the cosmological evolution of the dark matter. Secondly, we treat the weak freeze-out using the full kinetic equations instead of using an instantaneous approximation. Both improvements were shown to impact the Helium-4 prediction in the context of universally-coupled dark matter in previous work. We extend these lessons to more general couplings. We show that with these modifications, Big Bang Nucleosynthesis provides strong constraints of ultralight dark matter

with quadratic couplings to the Standard Model for a large range of masses as compared to other probes of this model, such as equivalence principle tests, atomic and nuclear clocks, as well as astrophysical and other cosmological probes.

Second, we examine equivalence principle (EP) violation experiments as a probe of quadratically coupled ULDM. EP tests are among the most sensitive experimental tools for detecting light, weakly coupled new physics. We revisit previous constraints from the MICROSCOPE experiment, correcting for a key omission: the effects of dark matter velocity dispersion. ULDM with quadratic couplings induces EP violation as follows. Interactions between ULDM and the Earth's matter generate an effective potential for the dark matter within the Earth, causing it to scatter and create a field gradient in the surrounding space. The same interactions induce a ϕ^2-dependent potential for Standard Model particles. If the couplings are not universal, these field gradients lead to forces that violate the equivalence principle. We show that velocity dispersion significantly modifies the resulting constraints. For ULDM masses above 10^{-11}, eV—where the de Broglie wavelength becomes comparable to or shorter than the MICROSCOPE-Earth distance—interference between incident and scattered waves enhances the signal, strengthening constraints for masses between 10^{-11} and 10^{-10}eV. For masses above 10^{-9}eV, destructive interference causes the constraints to weaken by orders of magnitude

Third, we outline the theoretical foundations of a forthcoming tabletop experiment designed to search for oscillating fundamental constants, as predicted by ULDM. These oscillations lead to periodic shifts in molecular absorption lines. Repeated measurements of a vibrational transition in hydrogen cyanide will enable a search for such signals.

This dissertation contains previously published as well as unpublished co-authored materials.

CURRICULUM VITAE

NAME OF AUTHOR: Thomas Bouley

GRADUATE AND UNDERGRADUATE SCHOOLS ATTENDED:

University of Oregon, Eugene, OR, USA
University of Cincinnati, Cincinnati, OH, USA

DEGREES AWARDED:

Doctor of Philosophy, Physics, 2025, University of Oregon
Bachelor of Science, Physics, 2019, University of Cincinnati
Bachelor of Science, Mathematics, 2019, University of Cincinnati

AREAS OF SPECIAL INTEREST:

Phenomenology of Ultralight Dark Matter
Cosmology
Astro-particle physics
Table top probes of BSM physics.

PROFESSIONAL EXPERIENCE:

Graduate Research Assistant, University of Oregon, 2019 – 2025
Graduate Teaching Assistant, University of Oregon, 2019 – 2025

GRANTS, AWARDS AND HONORS:

PUBLICATIONS:

T. Bouley, P. Sørensen, & T.-T. Yu *J. High Energ. Phys.* 104 (2023)

K. D. Holland, T. Bouley, & P. Horn *Ann Neurol.* 84: 1-9 (2018)

K. D. Holland, T. Bouley, & P. Horn *Epilepsia* 58: 1190-1198 (2017)

V. R. Santos, R. Y. K. Pun, S. R. Arafa, C. L. LaSarge, S. Rowley, S. Khademi, T. Bouley, K. D. Holland, N. Garcia-Cairasco, & S. C. Danzer *Neurobiology of Disease* 108: 339–351, (2017)

ACKNOWLEDGEMENTS

I am deeply grateful to my advisor, Tien-Tien Yu, for her guidance, encouragement for the freedom she gave me to explore my own ideas.

I thank everyone in the High-Energy Theory Group—Spencer Chang, Tim Cohen, Graham Kribs, Dave Soper, Tien-Tien Yu, Pouya Asadi, Ben Lillard, Cristien Arzate, Austin Batz, Layne Bradshaw, Joel Doss, Thomas Driscoll, Haidar Esseili, Carver Goldstein, Tom Gorordo, Gabriel Jacobo, Aria Radick, Ivan Juarez-Reyes, Thomas Schwemberger, and Tom Tong—for creating a vibrant community and for so many fun and productive discussions. I would also like the thank Anne McGinley, and Claire Staley for making IFS run smoothly and for letting me back into my office after I've locked myself out.

To all my fellow physics graduate students, thank you for the camaraderie and friendship that made these years joyful. I am especially grateful to Kehang Bai, Kevin Randles, Viola Lum, Austin Batz, Carver Goldstein, Cristien Arzate, Abhijeet Melkani, Haidar Esseili, Jennifer Lue, Aria Radick, Juliet Wright, Francesca Ark, and Scott Lambert for being such wonderful friends.

I also thank the physics undergraduates—Elise Jaremko and Owen Mitchem as well as the undergraduates Maylee Applegate, and Robin Mann—for their friendship.

To every past and present member of the Graduate Teaching Fellows Federation (GTFF): thank you for the countless hours you devoted—on top of graduate-school demands—to winning a better life for graduate employees and a better University of Oregon. Serving alongside you has been a privilege.

To the entire team that fought for our 2024–2026 contract, and especially the 2023–2024 bargaining team, thank you for your brilliance, determination, and

friendship. Working with you was the honor of my life. I am indebted to our lead negotiators, Cy Abbott and Emalydia Flenory, for their exceptional leadership. My thanks to the 2023–2024 GTFF Executive Board, who deftly led the union through strike preparations, and to the 2024–2025 Executive Board, who steered us through overlapping crises. Serving on both boards was an honor I will always cherish. Special thanks to Trevor Brunnenmeyer for bringing me into the GTFF and for his steadfast friendship. And special thank to Michael Marchman for over a decade of service, wisdom, and guidance to the GTFF. I am grateful to the GTFF Health and Welfare Trust for the insurance that saved me thousands of dollars in ER bills, and to Glenn Morris for keeping the Trust running smoothly.

My academic journey began with mentors who believed in me. Thank you to Alex Kagan for encouraging my self-study as an undergraduate and launching my interest in high-energy theory; to Paul Esposito, an extraordinary teacher who is missed by many; and to Fred Olness for urging me to pursue high-energy physics.

To Cory, thank you for so many engaging conversations—I hope you are doing well.

To my longtime friends Rishav Zamen, Audrey Schlembach, and Ann Wolf: thank you for more than a decade of unwavering friendship.

Above all, I thank my family for their love and support throughout my life. I love you.

There are surely people I have unintentionally omitted; please know that I am grateful to you as well.

Finally—and most importantly—I could not have finished graduate school without Nillawafer.

We must love one another or die

—From September 1, 1939 by W.H. Auden

TABLE OF CONTENTS

Chapter Page

LIST OF FIGURES

Figure Page

CHAPTER I

INTRODUCTION

This dissertation consists of three separate projects all of which involve constraining Ultralight Dark Matter.

Most of the matter in the Universe is not accounted for in the Standard Model (SM) of particle physics. This missing matter is referred to as dark matter (DM). Proposed candidates for DM range from many solar mass compact objects to ultralight DM with masses as low as about 10^{-19} eV [1, 2, 3]. In the low mass range, the DM is characterized by high occupation numbers, causing DM to behave like a classical field. Familiar examples of such ultralight DM (ULDM) are axion-like-particles [4, 5, 6] and dilatons (see, e.g., [7]). Dilatons are scalar fields ϕ present in models with compactified extra dimensions and have leading order couplings that are of the form [8]

$$\frac{\phi}{\Lambda}\mathcal{O}_{\rm SM}\,, \tag{1.1}$$

where $\mathcal{O}_{\rm SM}$ are terms in the SM Lagrangian and Λ is the scale of new physics generating the coupling. Scalars with such couplings generate new long-range forces, and such theories are, therefore, heavily constrained by 5th force experiments [9, 10, 11, 12]. In this work, we will consider instead scalar ULDM with quadratic couplings of the form

$$\frac{\phi^2}{\Lambda^2}\mathcal{O}_{\rm SM}\,, \tag{1.2}$$

which evades the most stringent constraints on dilatons and possesses novel phenomenology distinct from models with linear couplings. Such quadratic couplings can arise if the new physics assumed at the high-energy (UV) scale Λ is subject to symmetries that restrict the linear contributions. The lack of definitive observation of ULDM indicates that the ULDM must have extremely feeble couplings to ordinary matter. Beyond fifth-force searches, past attempts to search for ULDM have included searches for frequency variation of atomic clocks [13] and searches for perturbations in the arms of gravitational wave experiments [14]. Astrophysical probes of ULDM can be derived from Supernova SN1987A energy loss arguments [15, 16], from the spin-down of black holes due to superradiance [17, 18, 19, 20, 21, 22, 23], and from pulsar timing arrays [24, 25].

1.1 ULTRALIGHT DARK MATTER WITH QUADRATIC COUPLINGS

We begin by adding to the SM a real scalar field,

$$\mathcal{L}_\phi = \frac{1}{2}\partial_\mu\phi\partial^\mu\phi - \frac{1}{2}m_\phi^2\phi^2\,, \tag{1.3}$$

where m_ϕ is the scalar mass. The above Lagrangian is written with units where $c = \hbar = \epsilon_0 = k_B = 1$; units that we will use for the rest of the dissertation. Couplings, such as the ones considered below, will lead to corrections to the bare scalar mass. Generically, these are of the form

$$\delta m_\phi^2 \approx d_f^{(2)}\frac{m_f^2\Lambda_{\rm UV}^2}{M_{\rm pl}^2} \quad \text{coupling to fermions with mass } m_f, \tag{1.4}$$

$$\delta m_\phi^2 \approx d_b^{(2)}\frac{\Lambda_{\rm UV}^4}{M_{\rm pl}^2} \quad \text{coupling to bosons,} \tag{1.5}$$

with $\Lambda_{\rm UV}$ the scale of the UV completion and $d_i^{(2)}$ are dimensionless couplings defined below. Naïvely, m_ϕ, smaller than this correction could be considered unnatural because this contribution would have to be tuned out. However, there exist models in which these contributions are suppressed, e.g., see [26, 27]. Here, we seek to describe the phenomenology of such a field in a model-independent way, and we therefore leave any discussion of radiative corrections and protection from these to other work on model implementations.

We consider scenarios in which the scalar field is charged under a symmetry, e.g., $\mathbb{Z}_2$, such that the leading coupling is quadratic, *i.e.*, we take the interactions of the scalar with the SM to be in the form $\frac{\phi^2}{\Lambda^2}\mathcal{O}_{\text{SM}}$, where $\mathcal{O}_{\text{SM}}$ is a term in the SM Lagrangian and Λ is some high scale at which new physics appears. For ease of comparison with results in the literature, we will follow the conventions of [28, 8, 29, 30] and parameterize the interactions of the scalar particle with the SM with the following Lagrangian:

$$\mathcal{L} \supset 2\pi \frac{\phi^2}{M_{\text{pl}}^2}\left[\frac{d_e^{(2)}}{4e^2}F_{\mu\nu}F^{\mu\nu} - \frac{d_g^{(2)}\beta_3}{2g_3}G^A_{\mu\nu}G^{A\mu\nu} - d_{m_e}^{(2)} m_e \bar{e}e - \sum_{i=u,d}\left(d_{m_i}^{(2)} + \gamma_{m_i} d_g^{(2)}\right) m_i \bar{\psi}_i \psi_i\right]. \tag{1.6}$$

Here, $M_{\text{pl}} = 1.22 \times 10^{19}$ GeV is the Planck mass, β_3 is the QCD beta function, and γ_{m_i} are the anomalous dimensions of the u and d quarks. The superscript (2) specifies that these are the *quadratic* (as opposed to linear) couplings of the scalar. An alternative convention for parameterizing these coupling found in [31, 32, 33, 34, 35] has

$$\mathcal{L} \supset \frac{\phi^2}{\Lambda'^2_e}\frac{1}{4e^2}F_{\mu\nu}F^{\mu\nu} - \frac{\phi^2}{\Lambda'^2_g}\frac{\beta_3}{2g_3}G^A_{\mu\nu}G^{A\mu\nu} - \frac{\phi^2}{\Lambda'^2_{m_e}} m_e \bar{e}e - \sum_{i=u,d}\left(\frac{\phi^2}{\Lambda'^2_{m_i}} + \gamma_{m_i}\frac{\phi^2}{\Lambda'^2_g}\right) m_i \bar{\psi}_i \psi_i\,. \tag{1.7}$$

This convention implies that the scale of the new physics mediating these couplings to the SM is around Λ'. The conversion from this convention to the one used in this work is given by $d_i^{(2)} = \frac{M_{\text{pl}}^2}{2\pi\Lambda'^2_i}$ with $i = e, g, m_e, m_u,$ or m_d.

Note that the interactions defined in equation equation (1.6) will give rise to ϕ-dependency in the fundamental "constants" of the SM. In a background ϕ, the fundamental constants will shift according to

$$\frac{\Delta\alpha}{\alpha} = d_e^{(2)}\frac{\varphi^2}{2}\,, \tag{1.8}$$

$$\frac{\Delta\Lambda_{\rm QCD}}{\Lambda_{\rm QCD}} = d_g^{(2)}\frac{\varphi^2}{2}\,, \tag{1.9}$$

$$\frac{\Delta m_f}{m_f} = d_{m_f}^{(2)}\frac{\varphi^2}{2}, \quad \text{for } f = e, u, d, \tag{1.10}$$

where we have defined $\varphi = \frac{\sqrt{4\pi}\phi}{M_{\rm pl}}$. Here, $\alpha \simeq 1/137$ is the fine-structure constant, $\Lambda_{\rm QCD}$ the QCD confinement scale, and m_f are the fermion masses. The quark mass-couplings are more useful written in terms of the symmetric and antisymmetric combinations:

$$d_{\hat{m}}^{(2)} \equiv \frac{d_{m_d}^{(2)}m_d + d_{m_u}^{(2)}m_u}{m_d + m_u} \qquad \text{symmetric}, \tag{1.11}$$

$$d_{\delta m}^{(2)} \equiv \frac{d_{m_d}^{(2)}m_d - d_{m_u}^{(2)}m_u}{m_d - m_u} \qquad \text{anti-symmetric}, \tag{1.12}$$

as physical quantities come in these combinations. In particular, as will be discussed in **Chapter II**, the quark mass-couplings enter BBN through the neutron-proton mass difference, which depends on the anti-symmetric combination, and through the neutron axial coupling, which depends on the symmetric combination. Equivalence principle constraints will be the subject of **Chapter III** and are most sensitive to the absolute mass of the proton and neutrons which depends primarily on the symmetric quark coupling

CHAPTER II

VARYING FUNDAMENTAL CONSTANTS DURING BIG BANG NUCLEOSYNTHESIS WITH ULTRALIGHT DARK MATTER

This work was published in JHEP at [36] and was carried out in collaboration with Tien-Tien Yu and Phillip Sørensen. It was modified to fit into the format of a chapter for this dissertation.

In this chapter, we investigate cosmological probes of ULDM. Cosmology provides an attractive probe of ULDM because the field values of ULDM decrease with the expansion of the Universe, such that the largest field values are realized at early times. The earliest current probe of physics in the early Universe comes from Big Bang Nucleosynthesis (BBN), which therefore provides a powerful constraint of ULDM. This constraint appears because the presence of a background DM field can shift the effective value of fundamental constants and therefore can modify BBN [31]. To adequately model the effect of ultralight DM on BBN, the backreaction from the SM bath on the ULDM must be accounted for. Furthermore, the BBN analysis must go beyond instantaneous approximations of the neutron-proton, or weak, freeze-out. Previous work [37] has shown the relevance of these improvements in the context of universally-coupled ULDM. In this work, we investigate DM with more general couplings, correctly accounting for the evolution of the DM and the dynamics of weak freeze-out. We begin in section 1.1 with a description of the quadratically-coupled ULDM model and discuss the DM coupling to low-energy degrees of freedom. We also discuss the evolution of ULDM, properly accounting for the backreaction from the SM bath. In section 2.2, we provide an overview of BBN and show how ULDM affects BBN, specifically the predictions of the Helium-4 (^{4}He) abundance. In section 5.1

we will discuss the resulting constraints and compare the BBN constraints to other known constraints. We conclude in section 2.5.

2.1 DARK MATTER EVOLUTION

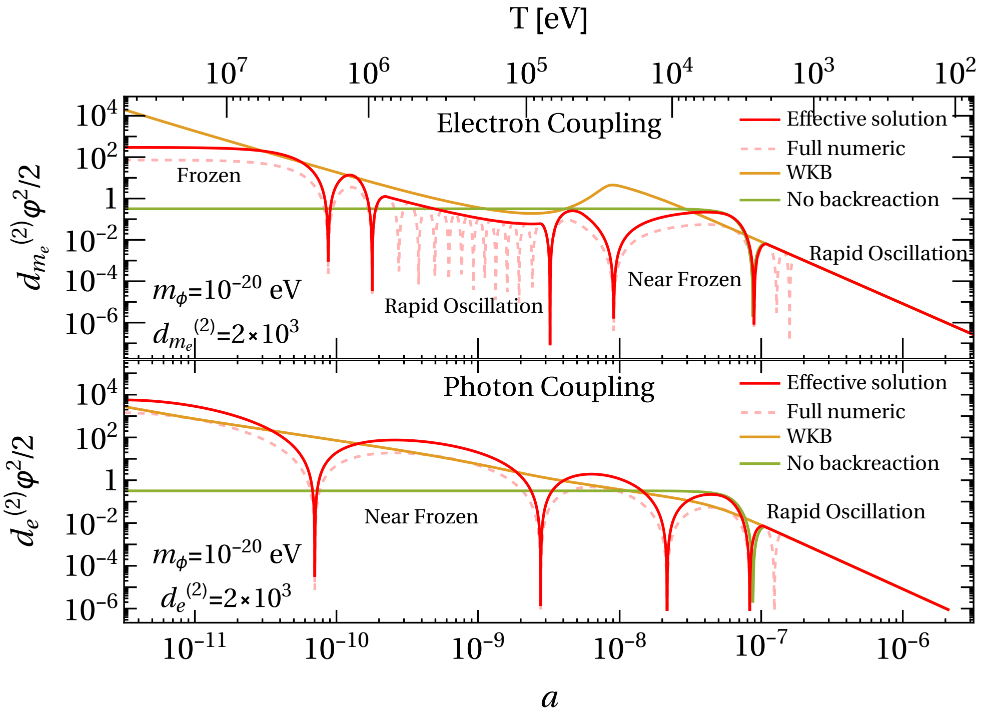

Figure 1. The evolution of the DM coupled to electrons (upper) or photons (lower). The effective solution is a splice of the numerical solution and the WKB approximation. The thermal mass used for the photon evolution was computed in the high-temperature limit as explained in section 2.1.2. The difference between the numerical solution and the effective solution in the non-oscillating regions is due to factors of 2 present in averaging. Time is indicated both in terms of temperature T and in terms of the scale factor a, the latter of which is normalized to $a_0 = 1$ today.

We are interested in the field values of the ULDM at BBN. The present-day field value, ϕ_0, is fixed by the current abundance of DM: $\rho_{\text{DM},0} = \frac{1}{2} m_\phi^2 \phi_0^2$. To determine the value of the field around BBN, we evolve the scalar field backward in time according to the homogenous Klein–Gordon equation in an expanding spacetime, using the present-day field value ϕ_0 as a boundary condition,

$$\ddot{\phi} + 3H\dot{\phi} + m_{\text{eff}}^2 \phi = 0\,, \tag{2.1}$$

where the $\dot{}$ denotes derivatives with respect to time, $H = \dot{a}/a$ is the Hubble rate, and a is the scale factor (normalized to $a_0 = 1$ today). The effective mass is a combination of the bare mass and the thermal mass induced by the SM bath: $m_{\text{eff}}^2 = m_\phi^2 + m_{\text{ind}}^2$. During BBN, the SM bath is primarily composed of photons, electrons, and neutrinos as these are the only species that are relativistic at the temperatures relevant for BBN. Thus, only interactions with photons ($d_e^{(2)}$) and electrons ($d_{m_e}^{(2)}$) give significant contributions to the thermal mass as other species are not sufficiently abundant[1]. Therefore, the quark ($d_{\delta m}^{(2)}$ and $d_{\hat{m}}^{(2)}$) and gluon ($d_g^{(2)}$) couplings do not provide a significant contribution to the thermal mass and the backreaction from these two couplings can be ignored.

To solve equation (2.1), we can examine three distinct regimes of DM evolution:

- Hubble friction domination (H): When $H^2 \gg m_{\text{eff}}^2$
- Bare mass domination (B): When $m_\phi^2 \sim m_{\text{eff}}^2 \gg H^2$
- Induced mass domination (I): When $m_{\text{eff}}^2 \gg H^2, m_\phi^2$

In the B and I regimes, ϕ is rapidly oscillating, and performing the full computation is numerically expensive. Instead, we model the interactions of the ULDM with matter by taking the average over an oscillation period. We use a WKB-type solution, as in [37], to find the amplitude of the oscillation. This WKB-type approximation gives,

$$\phi_{\text{amp}} \propto m_{\text{eff}}^{-1/2} a^{-3/2}, \tag{2.2}$$

where ϕ_{amp} is the amplitude of the rapidly oscillating ϕ. In the H regime, the field value is constant due to the Hubble friction term dominating the equation of motion. In the transitions between the regimes, the field is slowly oscillating and we can solve

---

[1] We do not consider couplings to neutrinos

the field evolution numerically and resolve the behavior of ϕ without the need for averaging. figure 1 shows an example evolution for $m_\phi = 10^{-20}\text{eV}$ and $d_e^{(2)} = 2000$ or $d_{m_e}^{(2)} = 2000$ comparing the evolution computed using our method to the pure WKB and numerical solution. In the top panel showing the electron coupling case the field transitions from being Hubble dominated at early times, to being induced mass dominated, and finally to being bare mass dominated. In the induced mass domination regime the field is slowly oscillating when the induced mass is comparable to the Hubble rate. We see the same behavior in the bottom panel, which shows the photon coupling case. We see that at early times the induced mass is comparable to Hubble and the field is slowly oscillating, and at late times it transitions to bare mass domination. In both panels, we see that at late times the field is rapidly oscillating, which is needed to satisfy the requirement that the field is DM today. The behavior shown in figure 1 is not generic and the evolution depends on the mass and couplings. As we see the induced mass is crucial to understand the behavior of the scalar field. In what follows, we discuss the induced thermal mass for the electron and photon couplings.

2.1.1 Electron coupling

There are two ways to calculate the induced mass from the interactions with electrons. The first is to calculate the induced mass using thermal field theory. The leading diagram is

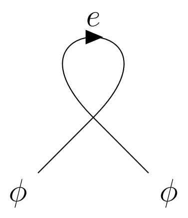

. (2.3)

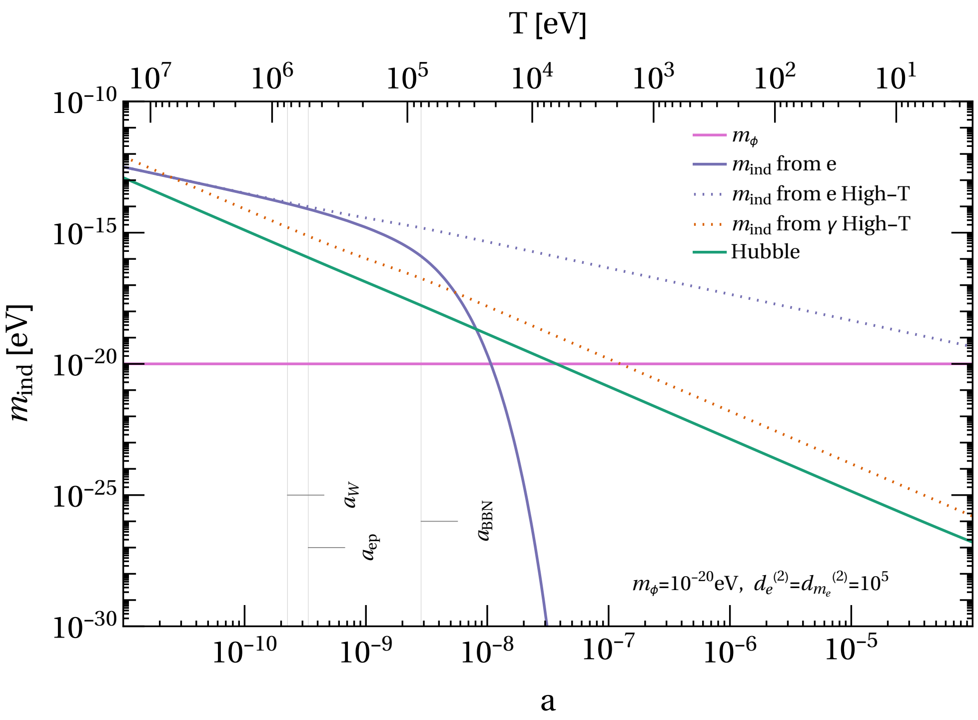

Figure 2. Potential contributions to m_{eff} from the electron and photon coupling for the couplings $d_e^{(2)} = 10^5$ or $d_{m_e}^{(2)} = 10^5$. The dotted lines are the high-temperature approximations for the electron and photon couplings, respectively.

In the imaginary time formalism described in [38, 39, 40, 41], this diagram gives

$$\Pi_1 = -2\frac{2\pi d_{m_e}^{(2)} m_e}{M_{\rm pl}^2} T \sum_{n=-\infty}^{\infty} \int \frac{{\rm d}^3 p}{(2\pi)^3} \frac{{\rm tr}(\not{p} + m_e)}{p^2 - m_e^2} \,, \tag{2.4}$$

where the sum is over the n Matsubara frequencies which each fix the time component of p to $p_0 = i(2n+1)T$. The temperature-dependent part of this diagram is given by

$$m_{\rm eff}^2 = m_\phi^2 + \frac{2\pi d_{m_e}^{(2)}}{M_{\rm pl}^2} \frac{4m_e^2}{\pi^2} T^2 \int_{m_e/T}^{\infty} {\rm d}x \frac{\sqrt{x^2 - (m_e/T)^2}}{e^x + 1} \,. \tag{2.5}$$

This calculation can be cross-checked with a second way of calculating the effective mass, which is to note that when electrons are on-shell the interaction $\frac{2\pi d_{m_e}^{(2)}}{M_{\rm pl}^2} \phi^2 m_e \bar{\psi}\psi$ can be written as $\frac{2\pi d_{m_e}^{(2)}}{M_{\rm pl}^2} \phi^2 \frac{i}{2}(\bar{\psi}\not{\partial}\psi - (\partial_\mu \bar{\psi})\gamma^\mu \psi) = \frac{2\pi d_{m_e}^{(2)}}{M_{\rm pl}^2} \phi^2 \Theta_e$ where Θ_e is the trace of the electrons' contribution to the stress-energy tensor. The effective mass is then given by [37, 42]

$$m_{\rm eff}^2 = m_\phi^2 + \frac{4\pi d_{m_e}^{(2)}}{M_{\rm pl}^2} \Theta_e = m_\phi^2 + \frac{4\pi d_{m_e}^{(2)}}{M_{\rm pl}^2} (\rho_e - 3P_e) \,, \tag{2.6}$$

which agrees with equation (2.5) after substituting

$$\rho_e = \frac{2}{\pi^2} T^4 \int_{m_e/T}^{\infty} {\rm d}x \frac{x^2 \sqrt{x^2 - (m_e/T)^2}}{e^x + 1}, \tag{2.7}$$

$$P_e = \frac{2}{3\pi^2} T^4 \int_{m_e/T}^{\infty} {\rm d}x \frac{(x^2 - (m_e/T)^2)^{3/2}}{e^x + 1}. \tag{2.8}$$

Note that for $T \gg m_e$, equation (2.5) implies that $m_{\rm eff}^2 \propto T^2$. In this regime, $m_{\rm eff}^2 \propto a^{-2}$ whereas $H^2 \propto a^{-4}$. Thus, at early times (high temperature), the DM evolution is dominated by Hubble friction and the field is in the H regime. Thus, the mass induced on ϕ from finite density effects can lead to highly non-trivial evolution of the scalar field. This can be seen in figure 2, where the induced mass $m_{\rm ind}^2 \equiv m_{\rm eff}^2 - m_\phi^2$ is compared to both H and the bare mass m_ϕ. In the example given in figure 2, which corresponds to the behavior also seen in figure 1, the field is initially dominated by Hubble friction, then starts oscillating because of the induced mass and the returns to a brief Hubble friction dominated state before finally settling into an oscillating state driven by the late time mass. figure 2 also shows the mass that can be induced by a photon coupling, which are discussed in the next section.

2.1.2 Photon coupling

For the photon coupling, we calculate the contribution to the induced mass using thermal field theory. The 1-loop diagram,

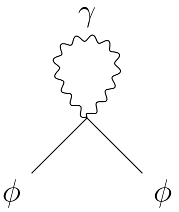

, (2.9)

gives

$$\Pi_1 = \frac{2\pi d^{(2)}_{m_e}}{M_{\mathrm{pl}}^2} T \sum_{n=-\infty}^{\infty} \int \frac{\mathrm{d}^3 p}{(2\pi)^3} (g^{\mu\nu} p^2 - p^\nu p^\mu) \frac{g_{\mu\nu}}{p^2} \,, \tag{2.10}$$

where similarly to equation (2.4) the sum is over the n Matsubara frequencies which set $p_0 = i2n\pi T$. This gives a scaleless integral and so vanishes in dimensional regularization, therefore this diagram does not contribute to the thermal mass. Instead, the leading diagram appears at two loops

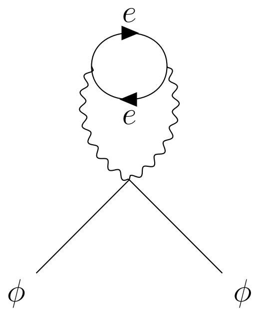

. (2.11)

This gives

$$\Pi_2 = \frac{2\pi d^{(2)}_{e}}{M_{\mathrm{pl}}} e^2 T \sum_{n=-\infty}^{\infty} \int \frac{\mathrm{d}^3 k}{(2\pi)^3} T \sum_{m=-\infty}^{\infty} \int \frac{\mathrm{d}^3 p}{(2\pi)^3} \Bigg(\frac{(g^{\mu\nu} k^2 - k^\mu k^\nu)(-1)\,\mathrm{tr}(\gamma_\mu(\not{p} + m_e)\gamma_\nu(\not{p} - \not{k} + m_e))}{k^4 (p^2 - m_e^2)((p-k)^2 - m_e^2)} \Bigg) \,, \tag{2.12}$$

summing over the n and m Matsubara frequencies which set $k_0 = i2n\pi T$ and $p_0 = i(2m+1)\pi T$. Evaluating the above expression is substantially complicated due to overlapping UV divergences, but it is relatively simple to compute in the limit where $T \gg m_e$. In this high-temperature limit, the contribution to the thermal mass is given by

$$\Pi_2 = \frac{2\pi d_e^{(2)}}{M_{\rm pl}^2} \frac{\alpha}{4\pi} \frac{\pi^2}{3} T^4 \,. \tag{2.13}$$

This high-temperature limit is a good approximation for the thermal mass at temperatures much larger than the electron mass. For lower temperatures, the finite electron mass suppresses the contribution. Therefore, we expect the high-temperature result to overestimate the thermal mass.

In the regime where the field is always oscillating, we expect this thermal mass contribution to somewhat relax the constraints. Therefore, the high-temperature result can be taken as conservative. This can be seen from the WKB-approximation, by which the amplitude of the oscillations can be described as $\phi \propto {m_{\rm eff}}^{-1/2} a^{-3/2}$. The thermal mass contribution decays in time, which then tends to compensate for the growth in a and therefore slow down the redshift of ϕ. This reduces the hierarchy between $\phi_{\rm BBN}$ and ϕ_0. Since ϕ_0 is fixed by the zero-temperature mass and the observed DM abundance today $\phi_{\rm BBN}$ will therefore be smaller in a scenario with thermal mass contribution, as long as WKB is always a good approximation of the evolution. This argument breaks down in the regime in which Hubble friction becomes significant and WKB approximation fails. In this regime, a thermal mass contribution can overcome Hubble friction which increases the strength of the constraint. At low m_ϕ the impact on the constraint is therefore a competition between opposing effects. For our purposes, we will present our results in the two limits using the high-temperature effective mass given in equation (2.13) and in the low-temperature limit where $m_{\text{eff}} \simeq m_\phi$, which provides an envelope within which the true bound will sit.

2.2 Ultralight Dark Matter and BBN

We are interested in understanding the effect of the ULDM couplings on the predictions of BBN. We, in section 2.2.1, begin with a brief review of the standard BBN analysis, following the discussion in [43]. From this, we can calculate an analytic estimate of the ^{4}He abundance. In section 2.3, we perturb the standard result to obtain constraints.

2.2.1 Standard BBN

The ^{4}He abundance is determined by the abundance of neutrons at the time that fusion to helium becomes efficient. This in turn is determined by the abundance of neutrons when neutrinos decouple and the time at which deuterium can form. Before weak freeze-out, the weak reactions $n + e^+ \leftrightarrow p + \bar{\nu}_e$ and $n + \nu_e \leftrightarrow p + e^-$ are efficient and neutrons and protons have equilibrium abundances,

$$X_n^{eq} = \frac{1}{1 + e^{m_{np}/T}} \,, \tag{2.14}$$

$$X_p^{eq} = 1 - X_n^{eq} = \frac{1}{1 + e^{-m_{np}/T}} \,, \tag{2.15}$$

where X_n^{eq} and X_p^{eq} are the equilibrium fractions of baryons in neutrons and protons, respectively, and m_{np} is the proton-neutron mass difference. As the Universe expands and cools, the reaction rate for these processes falls below the expansion rate of the Universe, the Hubble rate, and so the neutron abundance falls out of equilibrium. At this point, the evolution of the neutron abundance X_n is governed by the kinetic equation,

$$a\frac{\mathrm{d}X_n}{\mathrm{d}a} = -\frac{\lambda_{n\to p}}{H}(1 + e^{-m_{np}/T})(X_n - X_n^{eq}) \,, \tag{2.16}$$

where T is the temperature, and $\lambda_{n\to p}$ is the reaction rate of $n + (e^+ \text{ or } \nu) \to p + (\bar{\nu} \text{ or } e^-)$:

$$\lambda_{n\to p} = \frac{1 + 3g_{A_n}}{\pi^3} G_F^2 T^5 J\left(\frac{m_{np}}{T}\right) . \tag{2.17}$$

Here, G_F is the Fermi constant, g_{A_n} is the weak axial coupling, and J is a phase space factor, given by

$$J(z) = \frac{45\zeta(5)}{2} + \frac{21\zeta(4)}{2} z + \frac{3\zeta(3)}{2}\left(1 - \frac{m_e^2}{2m_{np}^2}\right) z^2 . \tag{2.18}$$

Solving equation (2.16) for the neutron abundance at late times gives

$$X_{n,W} = -\int_0^\infty \mathrm{d}a \frac{\mathrm{d}X_n^{eq}}{\mathrm{d}a} \exp\left[-\int_a^\infty \frac{\mathrm{d}a'}{a'} \tilde{\lambda}_{n\to p}\right] , \tag{2.19}$$

with $\tilde{\lambda}_{n\to p} = \frac{\lambda_{n\to p}}{H}(1 + e^{-m_{np}/T})$.

At this point, the neutron abundance continues to decrease due to neutron decay. The neutron abundance at these times follows

$$a\frac{\mathrm{d}X_n}{\mathrm{d}a} = -\frac{X_n \Gamma_n}{H} , \tag{2.20}$$

with Γ_n the neutron inverse lifetime given by

$$\Gamma_n = \frac{1 + 3g_{A_n}^2}{2\pi^3} G_F^2 m_e^5 P\left(\frac{m_{np}}{m_e}\right) , \tag{2.21}$$

where P is a phase space factor given by

$$P(x) = \frac{1}{60}\left((2x^4 - 9x^2 - 8)\sqrt{x^2 - 1} + 15x \ln\left(x + \sqrt{x^2 - 1}\right)\right) . \tag{2.22}$$

Integrating equation (2.20), we find the neutron abundance at BBN:

$$X_{n,BBN} = X_{n,W} \exp\left(-\int_{a_W}^{a_{BBN}} \frac{\mathrm{d}a}{aH}\Gamma_n\right) . \tag{2.23}$$

After weak freeze-out, neutrons and protons fuse to form deuterium through

$$p + n \leftrightarrow D + \gamma . \tag{2.24}$$

Initially, the photon abundance is much larger than the baryon abundance, and given that the deuterium binding energy is not very large compared to the temperature, equilibrium strongly favors the left side of equation (2.24). The deuterium abundance is given by the Saha equation

$$X_D = \frac{24\zeta(3)}{\sqrt{\pi}} \eta_b X_p X_n \left(\frac{T}{m_p}\right)^{3/2} e^{B_D/T}\,, \tag{2.25}$$

where $X_{p,n}$ is the abundance of protons and neutrons, respectively, B_D is the deuterium binding energy, and ζ is the Riemann zeta function. Note that the ^{4}He binding energy is much larger than B_D so in equilibrium ^{4}He would dominate. However, the reactions needed to form helium

$$\begin{aligned} \mathrm{D} + \mathrm{D} &\longleftrightarrow \mathrm{T} + \mathrm{p}\,, \\ \mathrm{D} + \mathrm{D} &\longleftrightarrow {}^3\mathrm{He} + \mathrm{n}\,, \\ \mathrm{D} + \mathrm{T} &\longleftrightarrow {}^4\mathrm{He} + \mathrm{n}\,, \\ \mathrm{D} + {}^3\mathrm{He} &\longleftrightarrow {}^4\mathrm{He} + \mathrm{p}\,, \end{aligned} \tag{2.26}$$

depend on the formation of deuterium and are suppressed by the low abundance of deuterium. This suppression of the deuterium abundance due to the background photons is known as the "deuterium bottleneck". Eventually when $T \approx \frac{B_D}{30}$, the deuterium abundance becomes large enough such that the reactions equation (2.26) become efficient. At this time most of the neutrons become bound into helium and the ^{4}He abundance is

$$Y_p \approx 2X_{n,BBN}\,. \tag{2.27}$$

Not long after this, the Universe becomes too cool and diffuse for these nuclear reactions to be efficient. This signals the end of BBN. After this, but before the onset of star formation, the tritium and ^{7}Be decay to ^{3}He and ^{7}Li respectively[2].

Equation equation (2.27) gives $Y_p \approx 0.25$ [43]. A detailed numerical calculation including the kinetics of the fusion reactions given in equation (2.26) gives $Y_p^{th} = 0.24672 \pm 0.00061$ using the baryon to photon ratio measured by Planck [45]. This is in excellent agreement with the PDG recommended average of $Y_p^{ex} = 0.245 \pm 0.003$ [1].

2.3 Effect of varying fundamental constants

We now consider how the presence of ULDM modifies the standard analysis above. We first consider how ϕ varies the fundamental constants and we then consider how this impacts the neutron fraction at freeze-out and at BBN. Finally, we derive the impact of ϕ on ^{4}He .

2.3.1 Variation in fundamental constants relevant for BBN

As we saw in the previous section, the ^{4}He abundance produced by BBN depends on the deuterium binding energy B_D, the proton-neutron mass difference m_{np}, and the neutron axial coupling g_A. In order to determine how the presence of ϕ affects BNN, one must determine how ϕ shifts m_{np}, B_D, and g_A. These parameters do not have analytic expressions but can only be calculated from first principles using lattice gauge theory. The shift in m_{np} and B_D can be estimated using a combination of lattice and analytic methods as discussed in [46]; we summarize the relevant parts below. The neutron-proton mass difference can be written as

$$m_{np} = m_n - m_p \approx b\alpha\Lambda_{\text{QCD}} + (m_d - m_u)\,, \tag{2.28}$$

---

[2] It should be noted that in the standard theory there was a discrepancy between predictions and observations of the ^{7}Li abundance. This is known as the *lithium problem*. However, the existence of this tension has recently been put into question [44].

where b is some constant number determined as in [46], giving $b\alpha\Lambda_{\rm QCD} \approx -0.76$MeV. Using equations equation (1.8), equation (1.9), and equation (1.10) we get

$$\frac{\Delta m_{np}}{m_{np}} = \frac{b\alpha\Lambda_{\rm QCD}}{m_{np}}\left(d_e^{(2)} + d_g^{(2)}\right)\frac{\varphi^2}{2} + \frac{m_d - m_u}{m_{np}}\left(d_{\delta m}^{(2)} + \gamma d_g^{(2)}\right)\frac{\varphi^2}{2}\,. \tag{2.29}$$

As already stated above, the dimensionless parameter φ is defined as $\varphi = \frac{\sqrt{4\pi}\phi}{M_{\rm pl}}$. The dependence of B_D on the fundamental constants can be parameterized as [46]

$$\frac{\Delta B_D}{B_D} = 18\frac{\Delta\Lambda_{\rm QCD}}{\Lambda_{\rm QCD}} = 18 d_g^{(2)}\frac{\varphi^2}{2}\,. \tag{2.30}$$

Determining the dependence of g_A on fundamental constants is more involved and requires input from lattice results. Lattice-QCD based attempts to estimate g_A from first principles have limited statistics for physical quark masses and rely on calculations at heavier quark masses to fit formulae taken from chiral perturbation theory (ChPT) to extrapolate to physical quark masses. To estimate the dependence of g_A on the quark masses we use these fits. Specifically, we use the expression

$$g_A(\epsilon_\pi) = g_0 - \epsilon_\pi^2\left((g_0 + 2g_0^3)\ln\epsilon_\pi - c_2\right) + g_0 c_3 \epsilon_\pi^3 \tag{2.31}$$

with $\epsilon_\pi = \frac{m_\pi}{4\pi f_\pi}$. This expression is from NNLO heavy baryon ChPT. It neglects effects from Δ resonances [47, 48] and is used by lattice groups for their extrapolation to physical quark masses [49, 50]. The coefficients g_0, c_2, and c_3 are determined from fits to lattice calculations. The dependence of g_A on ϵ_π can be used to infer the dependence on the quark masses using $m_\pi \propto \sqrt{\hat{m}}$ and neglecting the small dependence of f_π on the quark masses. Putting this all together, we have

$$\frac{\Delta g_A}{g_A} = d_{\hat{m}}^{(2)}\varphi\frac{1}{2}\frac{\partial \ln g_A}{\partial \ln \epsilon_\pi} \tag{2.32}$$

This depends on the specific values for the coefficients g_0, c_2, and c_3 that come from lattice fits. The values obtained from [51] and its supplementary materials are

$$g_0 = 1.237 \pm 0.034\,, \tag{2.33}$$

$$c_2 = -23.0 \pm 3.5\,, \tag{2.34}$$

$$c_3 = 28.7 \pm 5.5\,, \tag{2.35}$$

with the covariance matrix

$$\begin{array}{c|ccc} & g_0 & c_2 & c_3 \\ \hline g_0 & 0.011 & -0.12 & 0.18 \\ c_2 & -0.12 & 12.25 & -19.17 \\ c_3 & 0.18 & -19.17 & 30.25 \end{array}\,. \tag{2.36}$$

These give

$$\frac{\partial \ln g_A}{\partial \ln \epsilon_\pi} = -0.008 \pm 0.023\,. \tag{2.37}$$

Since the dependence of the ^{4}He abundance is proportional to $d^{(2)}_{\hat{m}} \frac{\partial \ln g_A}{\partial \ln \epsilon_\pi}$, and the interval above contains zero, we are not able to give meaningful constraints on $d^{(2)}_{\hat{m}}$ from BBN at this time. Improved lattice results may constrain $\frac{\partial \ln g_A}{\partial \ln \epsilon_\pi}$ away from 0, which in turn could give constraints on $d^{(2)}_{\hat{m}}$ from BBN.

Armed with these expressions that encode the effects of the ULDM on the parameters that enter the calculation for the ^{4}He abundance, we can now determine the effect of ULDM on the ^{4}He abundance.

2.3.1.1 Variation in the neutron abundance after weak freeze-out. We begin by varying equation (2.19) to find the change in $X_{n,W}$ due to the presence of ϕ (or equivalently to φ). To first order in $\kappa = d^{(2)}_i \frac{\varphi^2}{2}$, where $i = e, m_e, g,$ or δm, we find

$$\Delta X_{n,W} = -\int_0^\infty \mathrm{d}a \Bigg(\frac{\mathrm{d}X_n^{eq}}{\mathrm{d}a} \exp\Big[-\int_a^\infty \frac{\mathrm{d}a'}{a'}\tilde{\lambda}_{n\to p}\Big]\Big(-\int_a^\infty \frac{\mathrm{d}a'}{a'}\Delta\tilde{\lambda}_{n\to p}\Big) + \frac{\mathrm{d}\Delta X_n^{eq}}{\mathrm{d}a}\exp\Big[-\int_a^\infty \frac{\mathrm{d}a'}{a'}\tilde{\lambda}_{n\to p}\Big]\Bigg) \tag{2.38}$$

$$= -\int_0^\infty \mathrm{d}a \Bigg(\frac{\mathrm{d}X_n^{eq}}{\mathrm{d}a} \exp\Big[-\int_a^\infty \frac{\mathrm{d}a'}{a'}\tilde{\lambda}_{n\to p}\Big]\Big(-\int_a^\infty \frac{\mathrm{d}a'}{a'}\Delta\tilde{\lambda}_{n\to p}\Big) - \Delta X_n^{eq}\frac{\tilde{\lambda}_{n\to p}}{a}\exp\Big[-\int_a^\infty \frac{\mathrm{d}a'}{a'}\tilde{\lambda}_{n\to p}\Big]\Bigg) \tag{2.39}$$

$$= -\int_0^\infty \frac{\mathrm{d}a}{a}\exp\Big[-\int_a^\infty \frac{\mathrm{d}a'}{a'}\tilde{\lambda}_{n\to p}\Big]\Big(-\Delta X_n^{eq}\tilde{\lambda}_{n\to p} - a\frac{\mathrm{d}X_n^{eq}}{\mathrm{d}a}\int_a^\infty \frac{\mathrm{d}a'}{a'}\Delta\tilde{\lambda}_{n\to p}\Big)\,. \tag{2.40}$$

The change in $\Delta X_{n,W}$ depends on ΔX_n^{eq}, $\frac{\mathrm{d}X_n^{eq}}{\mathrm{d}a}$, and $\Delta\tilde{\lambda}_{n\to p}$. Let's first examine the variation in X_n^{eq}

$$\Delta X_n^{eq} = -\frac{m_{np}}{2T(1+\cosh m_{np}/T)}\frac{\Delta m_{np}}{m_{np}}\,, \tag{2.41}$$

and compare this to

$$a\frac{\mathrm{d}X_n^{eq}}{\mathrm{d}a} = -\frac{m_{np}}{2T(1+\cosh(m_{np}/T))}\,. \tag{2.42}$$

The variation in $\tilde{\lambda}_{n\to p}$ is given by

$$\frac{\Delta\tilde{\lambda}_{n\to p}}{\tilde{\lambda}_{n\to p}} = \frac{\Delta\lambda_{n\to p}}{\lambda_{n\to p}} - \frac{m_{np}X_n^{eq}}{T}\frac{\Delta m_{np}}{m_{np}}\,, \tag{2.43}$$

with the variation in $\lambda_{n\to p}$ given by

$$\frac{\Delta\lambda_{n\to p}}{\lambda_{n\to p}} = \frac{6g_{A_n}^2}{1+3g_{A_n}^2}\frac{\Delta g_{A_n}}{g_{A_n}} + 2\frac{\Delta G_F}{G_F} + \frac{\Delta(J(m_{np}/T))}{J(m_{np}/T)} \tag{2.44}$$

$$= \frac{6g_{A_n}^2}{1+3g_{A_n}^2}\frac{\Delta g_{A_n}}{g_{A_n}} + 2\frac{\Delta G_F}{G_F} + \frac{m_{np}J'}{TJ}\frac{\Delta m_{np}}{m_{np}} - \frac{3\zeta(3)}{2J}\frac{m_e^2}{T^2}\frac{\Delta m_e}{m_e} + \frac{3\zeta(3)}{2J}\frac{m_e^2}{T^2}\frac{\Delta m_{np}}{m_{np}}\,. \tag{2.45}$$

The last two terms in equation (2.45) are proportional to $\frac{m_e^2}{T^2}$, which is small at relevant times and in principle can be neglected. However, we will include them going forward.

Note that $\frac{\Delta G_F}{G_F} = 0$ for the models we are considering. Putting everything together we find that the change in the neutron abundance at weak freeze-out is given by

$$\boxed{\begin{aligned} \Delta X_{n,W} = \int_0^\infty \frac{\mathrm{d}a}{a} \frac{m_{np}}{2T(1+\cosh(m_{np}/T))} \exp\Big[- \int_a^\infty \frac{\mathrm{d}a'}{a'} \tilde{\lambda}_{n\to p} \Big] \\ \times \Big\{ - \tilde{\lambda}_{n\to p} \frac{\Delta m_{np}}{m_{np}} + \int_a^\infty \frac{\mathrm{d}a'}{a'} \tilde{\lambda}_{n\to p} \Big[\frac{m_{np} X_n^{eq}}{T} \frac{\Delta m_{np}}{m_{np}} \\ - \frac{6 g_{A_n}^2}{1+3g_{A_n}^2} \frac{\Delta g_{A_n}}{g_{A_n}} - 2 \frac{\Delta G_F}{G_F} - \frac{m_{np} J'}{TJ} \frac{\Delta m_{np}}{m_{np}} \\ + \frac{3\zeta(3)}{2J} \frac{m_e^2}{T^2} \left(\frac{\Delta m_e}{m_e} - \frac{\Delta m_{np}}{m_{np}} \right) \Big] \Big\}. \end{aligned} \qquad (2.46)}$$

2.3.2 Variation in the neutron abundance at BBN

After weak freeze-out, the neutron abundance is modified by neutron decay. To find the variation in the neutron abundance at BBN, we vary equation (2.23) to find

$$\frac{\Delta X_{n,BBN}}{X_{n,BBN}} = \frac{\Delta X_{n,W}}{X_{n,W}} - \left(\int_{a_W}^{a_{BBN}} \frac{\mathrm{d}a}{aH} \Delta\Gamma_n \right) - \frac{\Gamma_n}{H} \frac{\Delta a}{a} \Big|_{a_W}^{a_{BBN}} \tag{2.47}$$

$$\approx \frac{\Delta X_{n,W}}{X_{n,W}} - \left(\int_{a_W}^{a_{BBN}} \frac{\mathrm{d}a}{aH} \Delta\Gamma_n \right) + \frac{\Gamma_n}{H} \Big|_{a_{BBN}} \frac{\Delta T_{BBN}}{T_{BBN}}, \tag{2.48}$$

where we dropped the $\frac{\Delta T_W}{T_W}$ term because at weak freeze-out $\frac{\Gamma_n}{H} \ll 1$. The variation in the neutron lifetime is given by

$$\frac{\Delta\Gamma_n}{\Gamma_n} = \frac{6 g_{A_n}^2}{1+3g_{A_n}} \frac{\Delta g_{A_n}}{g_{A_n}} + 2 \frac{\Delta G_F}{G_F} + 5 \frac{\Delta m_e}{m_e} + \frac{m_{np} P'}{m_e P} \left(\frac{\Delta m_{np}}{m_{np}} - \frac{\Delta m_e}{m_e} \right). \tag{2.49}$$

2.3.3 Variation in the helium abundance

The variation of equation (2.27) gives

$$\frac{\Delta Y_p}{Y_p} = \frac{\Delta X_{n,BBN}}{X_{n,BBN}}. \tag{2.50}$$

The remaining piece of our calculation is to determine $\frac{\Delta T_{BBN}}{T_{BBN}}$. Recall that the time of BBN is determined by the deuterium abundance reaching a critical value allowing the efficient fusing of deuterium into ^{4}He . Using equation (2.25), we can find T_{BBN} by examining

$$X_D^{\mathrm{crit}} = \frac{24\zeta(3)}{\sqrt{\pi}} \eta_b (1 - X_{n,BBN}) X_{n,BBN} \left(\frac{T_{BBN}}{m_p} \right)^{3/2} e^{B_D/T_{BBN}} \,. \tag{2.51}$$

Note that the left-hand side is exponentially dependent on B_D/T_{BBN}. Therefore, any shift in B_D must be compensated by a shift in T_{BBN}, indicating that T_{BBN} depends mostly on B_D, i.e.

$$\frac{\Delta T_{BBN}}{T_{BBN}} \approx \frac{\Delta B_D}{B_D} \,. \tag{2.52}$$

Combining everything, we get

$$\boxed{\begin{aligned} \frac{\Delta Y_p}{Y_p} = \frac{\Delta X_{n,W}}{X_{n,W}} + \frac{\Gamma_n}{H} \frac{\Delta B_D}{B_D} \bigg|_{a_{BBN}} - \int_{a_W}^{a_{BBN}} \frac{\mathrm{d}a}{a} \frac{\Gamma_n}{H} \bigg(& \frac{6 g_{A_n}^2}{1 + 3 g_{A_n}} \frac{\Delta g_{A_n}}{g_{A_n}} \\ & + 2 \frac{\Delta G_F}{G_F} + 5 \frac{\Delta m_e}{m_e} + \frac{m_{np} P'}{m_e P} \left(\frac{\Delta m_{np}}{m_{np}} - \frac{\Delta m_e}{m_e} \right) \bigg) \,. \end{aligned}} \tag{2.53}$$

Using equations (1.10), (2.29) and (2.30) for the variations in the fundamental constants we can now find the change in the ^{4}He abundance in terms of the field value of ϕ as a function of redshift. ϕ as a function of redshift was found using the evolution as described in section 2.1. We place constraints on the DM couplings by requiring that the resulting shift in the ^{4}He abundance keeps the ^{4}He abundance in the 95% confidence interval of the observed abundance, *i.e.* we require that $Y_p^{ex} - Y_p^{th} - 2\sigma_{Y_p} < \Delta Y_p < Y_p^{ex} - Y_p^{th} + 2\sigma_{Y_p}$ with σ_{Y_p} being the uncertainty of the theory prediction and the experimental uncertainty added in quadrature. We use the values $Y_p^{ex} = 0.245$, $Y_p^{th} = 0.24672$, and $\sigma_{Y_p} = 0.012$ from [1] and [45].

2.4 Results

The constraints on quadratically-coupled ULDM obtained from BBN in this work are shown as solid red lines in figure 3. For masses larger than about 10^{-14} eV, the evolution is in the bare mass dominated regime both during and after weak freeze-out. For these masses, the constraints scale as $d_i^{(2)} \propto m_\phi^2$ regardless of coupling. For the quark and gluon couplings, the field is Hubble frozen before BBN for masses lower than 10^{-19}eV. This leads the constraint to scale as $d_i^{(2)} \propto m_\phi^{1/2}$ in this low-mass regime. At intermediate masses, the field is Hubble frozen-in during or between weak freeze-out and BBN and the behavior is more complicated. For the electron coupling, the thermal mass is relevant for the evolution of the dark matter for masses less than 10^{-18}eV. This leads to slow oscillations on the timescale of relevant BBN dynamics and the complex behavior shown in figure figure 3. For the photon coupling, we show two different constraints for two different estimates of the effective mass. The dark red line neglects the thermal mass of ϕ and the red line uses the thermal mass calculated in the high-temperature limit. We expect that the true constraint, calculated using the exact thermal mass, would be in between these two bounds as explained in section 2.1.2.

The BBN constraints derived in this work improve on the constraints derived in [31] by including the effects of the thermal mass on the evolution of the dark matter and by treating weak freeze-out using the full kinetic description. For the electron coupling, at masses of at least $m_\phi \gtrsim 10^{-14}$eV the two effects lead to a constraint about two orders of magnitude weaker than the constraint given in [31]. This reduced constraint is explained by the thermal mass which reduces the field value at the BBN era. For the quark coupling, the thermal mass is insignificant and the constraint on this coupling is instead enhanced by about a factor 2 relative to

[31] in the $m_\phi \gtrsim 10^{-14}$eV regime. In all cases, for masses below 10^{-14}eV we see nontrivial behavior not seen in [31]. For the photon coupling, our results indicate only the region of parameter space in which a full calculation of the thermal effects is expected to place the constraint. The constraint on the photon coupling given in [31] lies within the region where we expect the constraint to lie. Therefore, we cannot show a change in the photon coupling constraint without a more detailed evaluation of thermal effects, which we leave to future work. The gluon coupling was not treated in [31] and thus the constraints on the gluon coupling derived in this work are completely novel.

Our analysis is valid in the regime where $d_i^{(2)}\varphi^2 \ll 1$. In this regime, we can neglect the higher-order interactions of ϕ with the SM that would be present in a UV completion and treat ϕ as a small perturbation to the SM. Importantly, we can neglect the effect of the thermal quartic and other higher-order terms on the evolution of the ULDM. Because the amplitude of ϕ decreases with redshift, the threshold $d_i^{(2)}\varphi^2 \sim 1$ could have been crossed sometime in the early Universe; if this happens after weak freeze-out then details of the UV completion are needed to determine the impact of ϕ on BBN. The parameter space in which the condition that $d_i^{(2)}\varphi^2 \ll 1$ is violated at any time after weak freeze-out corresponds to the lightly shaded regions above the dashed red lines in figure 3. In these regions, a model-dependent treatment is required for any given UV completion.

2.5 Conclusions

In this chapter, we examined the effect of ultralight scalar DM with quadratic couplings on the predicted helium abundance produced by Big Bang nucleosynthesis. Figure 3 shows the constraints derived in this chapter. In addition, we also show constraints from the Eöt-Wash and MICROSCOPE experiments, atomic clocks experiments, and projected constraints from the AION and AEDGE matter-wave interferometry experiments. In this chapter, we treated weak freezeout in the full kinetic description and accounted for backreaction from the SM on the evolution of the DM. From the impact of ULDM on BBN, we constrain the couplings of ULDM to electrons, quarks, and photons for DM masses ranging from about 10^{-19}eV to 10^{-4}eV. This updates the result in [31] that treated weak freezeout in the instantaneous approximation and neglected backreaction from the SM on the evolution of the DM. For a significant range of parameter space, we show that the bounds from BBN are the strongest constraints on quadratically coupled ultra-light dark matter. We show that these BBN bounds are significantly modified by the effects of the backreaction and the full kinematic decoupling studied in this chapter.

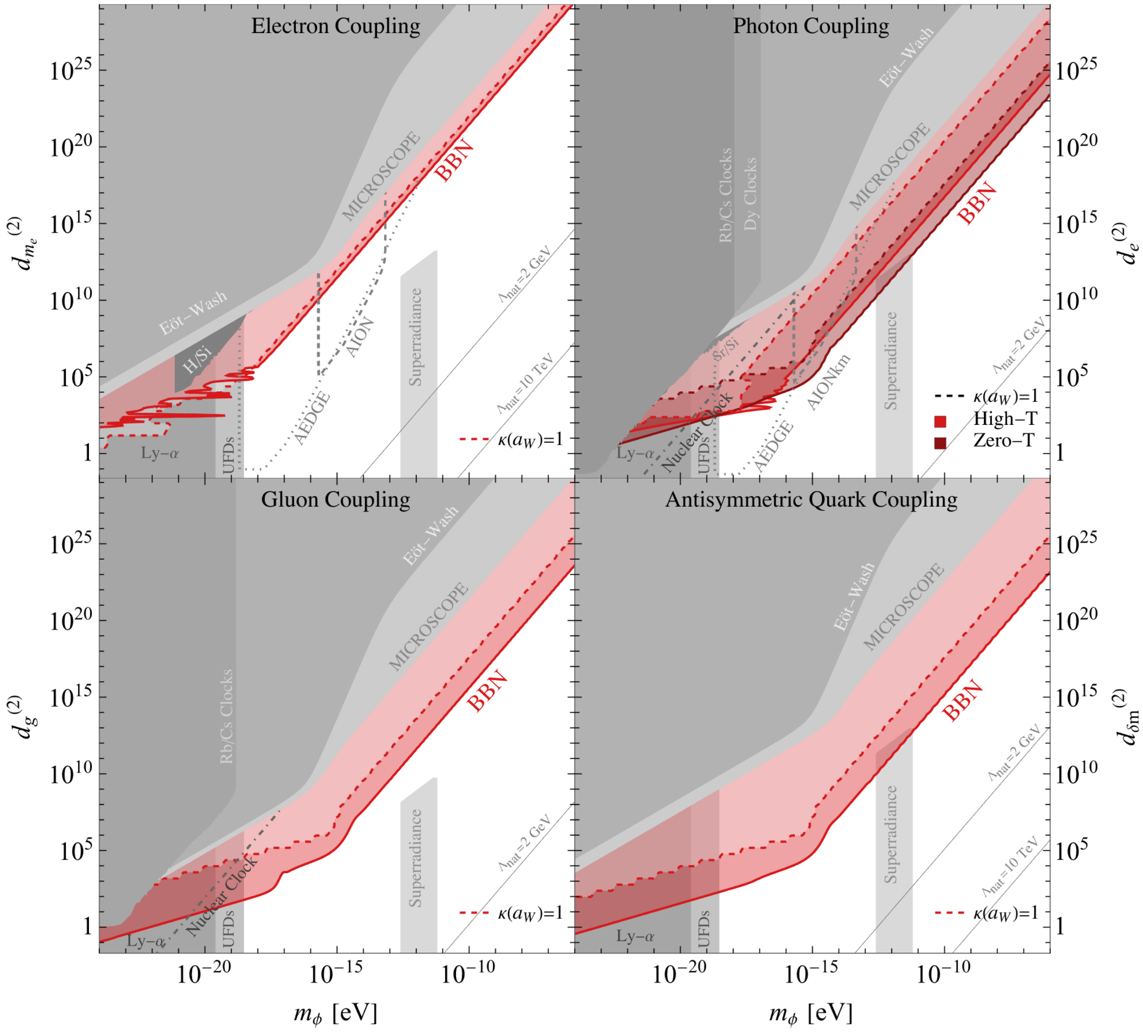

Figure 3. Constraints on quadratic couplings of ULDM to electrons, quarks, gluons, and photons. Red regions indicate the BBN constraints derived in this paper. Other constraints are given in shades of gray. On the photon coupling plot, the conservative high-temperature approximation of the thermal mass yields the constraint in lighter red while the optimistic zero-temperature (i.e., without backreaction) result yields the constraint in darker red, see section 2.1.2 for details. The dashed red lines indicate where the approximation used in this paper breaks down and a more detailed analysis is needed. The grey regions show parameter space ruled out by prior work from the Eöt-Wash [9] and MICROSCOPE [52] experiments, atomic clock experiments [53, 29] as well as constraints from Lyman-α [2], UFDs [3] and superradiance [23, 54]. Also shown, with dashed gray lines, are projected constraints from the AION and AEDGE experiments [55, 56] as well as projections for nuclear clocks [57]. Following the discussion in section 1.1, we show the line above which the low values of m_ϕ may be rendered unnatural by large loop corrections, assuming a cutoff of $\Lambda = 10$ TeV and $\Lambda = 2$ GeV. For the gluon and photon plots, the line for a $\Lambda = 10$ TeV cutoff lies outside the range shown.

CHAPTER III

UPDATING EQUIVALENCE PRINCIPLE TEST OF ULTRALIGHT DARK MATTER

The work presented in this chapter was carried out in collaboration with Tien-Tien Yu.

3.1 Introduction

The equivalence principle (EP) states that all objects fall at the same rate of acceleration, regardless of their mass or composition. Tests of the EP, also known as the universality of free fall, have confirmed the predictions of general relativity to remarkable precision, and therefore provide stringent constraints on the existence of new "fifth-forces." The existence of beyond the Standard Model (BSM) physics can also contribute to violations of the EP. As such, EP tests have been utilized to great success at constraining BSM physics. In particular, EP tests have ruled out large swaths of parameter space for ultralight scalars that couple to the SM.

In this work, we are interested in understanding the effects of ultralight quadratically-coupled scalar dark matter (DM) on equivalence principle tests. Ultralight DM are dark matter candidates at the lower end of the allowed DM mass ranges, with masses less than about 1eV. At these masses, the occupation number of particles in a de Broglie volume of the DM is large and the collection of particles act coherently. In this regime, the DM behaves like a wave and is well-described by classical field equations.

Previous works constraining quadratically-coupled ultralight scalar DM with equivalence principle experiments have adopted a simplifying assumption that the DM is a homogeneous field at distances far from the Earth and neglected velocity dispersion effects of the DM. This is a valid approximation for dark matter masses below 10^{-10} eV, because in this range the typical de Broglie wavelength of the DM is large compared to the radius of the Earth and so the DM field appears homogeneous on the relevant scales. We show this explicitly in appendix A.2.2. For dark matter masses above this scale, the typical de Broglie wavelength of the dark matter is small compared to the radius of the Earth, and so the assumption that the field is homogeneous breaks down. In this work, we expand on this last point and demonstrate how the velocity dispersion can have important effects on the EP constraints on ultralight scalar DM. These effects are important, in particular, for any space-based experiment searching for quadratically-coupled ultralight scalars.

The chapter is organized as follows firstly, in section 3.2, we review equivalence principle experiments and how quadratically coupled ultralight dark matter can cause apparent equivalence principle violation. Then, in section 3.3, we discuss the dark matter velocity dispersion that we show is necessary to correctly calculate the constraints form equivalence principle violation searchers. We then detail the calculation of the dark matter the wave function that is critical for the derivation of constraints from equivalence principle experiments in section 3.4. Next, in section 3.5, we discuses the effects dark matter wind that we had neglected in the forgoing chapters. Then we review the qualitative features of the results in section 3.6 before concluding in section 3.7.

3.2 Equivalence Principle Tests

The weak equivalence principle states that all small test bodies, influenced only by gravity, accelerate at the same rate regardless of their composition. This principle is foundational to general relativity, reflecting the geometric nature of gravity. Tests of the weak equivalence principle typically fall into two categories:

- In the conceptually simplest setup, two test bodies are placed in free fall, and their gravitational accelerations are directly compared. This type of experiment is commonly employed in space-based equivalence principle tests.

- The other type, known as Eötvös-type experiments, compares the gravitational mass of two test bodies against their inertial masses using torsion balances or similar devices.

Although equivalence principle tests are often interpreted as tests of general relativity itself, they can equivalently be seen as searches for novel, composition-dependent non-gravitational forces. Modern EP tests achieve sensitivity to forces roughly 13 orders of magnitude weaker than gravity [58], placing strong constraints on potential new scalar or vector fields mediating long-range interactions.

Quadratically coupled ultralight dark matter, as detailed in Section 1.1, can generate precisely such composition-dependent forces. This arises because atomic masses depend sensitively on both the masses of constituent particles and their binding energies, each of which is influenced by fundamental constants. The couplings discussed previously lead these constants to depend explicitly on the dark matter field value, resulting in mass shifts proportional to φ^2 as described by equations (1.8)-(1.10). Because of the dependence of the mass on φ^2, moving an object from a region of low φ^2 to one of high φ^2 requires work. In other words, φ^2 acts as a potential for the object, which leads to a force and therefore an induced acceleration. Thus, variations in the local dark matter field translate directly into observable signals in equivalence principle violation tests. To quantify how sensitively the mass of an object A depends on φ, we introduce the coupling $\alpha_A^{(2)}$ as follows

$$\frac{\Delta m_A}{m_A} = \frac{1}{2}\alpha_A^{(2)}\varphi^2 \,. \tag{3.1}$$

This coupling, $\alpha_A^{(2)}$, explicitly relates to the fundamental couplings introduced in equation (1.6) and can be expressed as [8]:

$$\begin{aligned}\alpha_A^{(2)} = d_g^{(2)} &+ [Q_{m_e}]_A\,(d_{m_e}^{(2)} - d_g^{(2)}) \\ &+ [Q_{\hat{m}}]_A\,(d_{\hat{m}}^{(2)} - d_g^{(2)}) \\ &+ [Q_{\delta m}]_A\,(d_{\delta m}^{(2)} - d_g^{(2)}) \\ &+ [Q_e]_A\,d_e^{(2)}\end{aligned} \tag{3.2}$$

where the $[Q_i]_A$ are the dilatonic charges specific to object A, derived explicitly in [8]. For a pure element with atomic number Z and mass number A, these charges are approximately:

$$[Q_e]_A = 10^{-4} \times F_A \left[-1.4 + 8.2\frac{Z}{A} + 7.7\frac{Z(Z-1)}{A^{4/3}}\right] , \tag{3.3}$$

$$\begin{aligned}[Q_{\hat{m}}]_A = F_A \Bigg[0.093 - \frac{0.036}{A^{1/3}} - 0.02\frac{(A-2Z)^2}{A^2} \\ -1.4 \times 10^{-4}\frac{Z(Z-1)}{A^{4/3}}\Bigg] ,\end{aligned} \tag{3.4}$$

$$[Q_{\delta m}]_A = F_A \left[0.0017\frac{A-2Z}{A}\right] , \tag{3.5}$$

$$[Q_{m_e}]_A = F_A \left[5.5 \times 10^{-4}\frac{Z}{A}\right] , \tag{3.6}$$

with $F_A = A\frac{931\ \text{MeV}}{m_A} = 1 + \mathcal{O}(10^{-4})$.

The induced potential from the φ-dependence of m_A is of the form

$$V(\varphi) = m_A \frac{1}{2}\alpha_A^{(2)}\varphi^2 . \tag{3.7}$$

The acceleration due to this potential is then given by

$$\vec{a}_A = -\vec{\nabla}V(\varphi)/m_A = -\alpha_A^{(2)}\varphi\vec{\nabla}\varphi . \tag{3.8}$$

Since φ couples *quadratically* to matter, φ gets an effective mass in the presence of matter. This induced mass is given by

$$m_{\text{ind}}^2(x) = \alpha^{(2)}(x)4\pi G\rho(x) , \tag{3.9}$$

with $\rho(x)$ the matter density and $\alpha^{(2)}(x)$ is similar to $\alpha_A^{(2)}$ except for a small volume at x. In general the induced mass depends on the position so φ obeys the Klein-Gordon equation with a position dependent mass

$$\Box\varphi + m_{\text{eff}}^2(x)\varphi = 0\,, \tag{3.10}$$

with $m_{\text{eff}}^2(x) = m_\varphi^2 + m_{\text{ind}}^2(x)$.

These composition dependent accelerations given in eq. 3.8 can be directly probed by EP experiments such as the MICROSCOPE mission [59, 60]. One such measurement was made by the MICROSCOPE space mission [59, 60]. In this mission, two test masses made of alloys of Pt and Ti were placed in a satellite which was in a nearly circular orbit around the Earth at 710 km of altitude. At this altitude, the Earth's gravitational acceleration is about 7.9 m/s^2. A violation of the equivalence principle would manifest itself as a differential acceleration between the two test masses. The constraints from this mission found a limit on the Eötvos parameter,

$$\begin{aligned}
\eta_{Pt-Ti,\oplus} &= 2\frac{|\vec{a}_{Pt} - \vec{a}_{Ti}|}{|\vec{a}_{Pt} + \vec{a}_{Ti}|} && (3.11)\\
&= \frac{r^2\Delta\alpha^{(2)}\hat{r}\cdot\langle\varphi\vec{\nabla}\varphi\rangle}{GM_\oplus} && (3.12)\\
&= \frac{\Delta\alpha^{(2)}\hat{r}\cdot\langle\varphi\vec{\nabla}\varphi\rangle}{7.9\ \text{m/s}^2} && (3.13)\\
&= (-0.1 \pm 1.3)\times 10^{-14}\,. && (3.14)
\end{aligned}$$

The remainder of this paper is on the calculation of η, which as we see depends on $\hat{r}\cdot\varphi\vec{\nabla}\varphi$.

3.3 Dark Matter Distribution

To solve equation (3.10) for φ we must stipulate appropriate boundary conditions. Far from massive bodies such as the Earth, the field oscillates about 0 with frequency m_φ; however, its amplitude and phase vary because of the dark-matter velocity distribution [61]. Since these fluctuations are intrinsically unpredictable, we regard the field as a single realization drawn from a statistical ensemble. It is shown is [61] that the correct ensemble is an ensemble of plane waves that are incident to the Earth. All of the needed information about the distribution can be extracted from the two point function which is given by

$$\langle\varphi(t,\vec{x})\varphi(t',\vec{x}')\rangle = \frac{\varphi_0^2}{2}\int\frac{\mathrm{d}^3v}{\gamma(v)}g(\vec{v})\Re(\varphi_{\vec{v}}(t,\vec{x})\varphi^*_{\vec{v}}(t',\vec{x}'))\,, \tag{3.15}$$

with φ the dark matter amplitude determined by the local dark matter density according to $\varphi_0 = \sqrt{\frac{8\pi G\rho_\varphi}{m_\varphi^2}}$; $g(\vec{v})$ is the velocity distribution of the dark matter; $\gamma(v) = \frac{1}{\sqrt{1-v^2}}$ because dark matter is non relativistic $\gamma(v) \approx 1$ on the support of g; and $\varphi_{\vec{v}}$ the solution to equation 3.10 with the income plane wave with velocity $\vec{v}$ scattering off of the Earth.

From equation (3.15) it is straightforward to compute $\langle\varphi\,\vec{\nabla}\varphi\rangle$, which enters the evaluation of η in section 3.2. Consequently, the calculation of η reduces to solving the scattering problem described above.

3.4 Calculating the Dark Matter Wave Function

To solve this scattering problem we express the general solution of 3.10 in a basis of incoming and outgoing spherical waves and match them to the incoming part of $e^{i\vec{x}\cdot\vec{p}}$ with $\vec{p} = \gamma\vec{v}m_\varphi$. We start with expanding the $\Box$ in eq. 3.10, which gives

$$\partial_t^2\varphi - \nabla^2\varphi + m_{\text{eff}}^2(\vec{x})\varphi + = 0\,. \tag{3.16}$$

We can solve this using separation of variables by writing $\varphi(t,\vec{x}) = T(t)X(\vec{x})$. This results in

$$\ddot{T} - \omega^2 T = 0 \tag{3.17}$$

$$\nabla^2 X + k_{\text{eff}}^2(\vec{x})X = 0 \tag{3.18}$$

with $k_{\text{eff}}^2(\vec{x}) = \omega^2 - m_{\text{eff}}^2(\vec{x})$. The solution to eq. 3.17 is given by $T = e^{\pm i\omega t}$. We then take the simplifying approximation that the Earth is a sphere of uniform density. This allows us to write eq. 3.18 as

$$\nabla^2 X + [k_0^2 - \alpha_\oplus^{(2)} 4\pi G\rho_\oplus \theta(R_\oplus - r)]X = 0 \tag{3.19}$$

with $k_0^2 = \omega^2 - m_\varphi^2$. The goal now is to solve for X.

We solve eq. 3.19 with separation of variables writing $X(\vec{x}) = R(|\vec{x}|)Y(\hat{x})$. The angular equation is solved by spherical harmonics $Y(\hat{x}) = Y_l^m(\hat{x})$. The radial equation is

$$\frac{1}{r^2}\frac{d}{dr}\left(r^2\frac{dR}{dr}\right) - \frac{l(l+1)}{r^2}R + k_0^2 + (k_\oplus^2 - k_0^2)\theta(R_\oplus - r)R = 0\,, \tag{3.20}$$

with $r = |\vec{x}|$ and $k_\oplus^2 = k_0^2 - \alpha_\oplus^{(2)} 4\pi G\rho_\oplus$. This has the general solution

$$R_l(r) = \begin{cases} \frac{1}{2}[C_l h_l^{\text{in}}(k_0 r) + A_l h_l^{\text{out}}(k_0 r)] & r < R_\oplus \\ B_l j_l(k_\oplus r) & r > R_\oplus \end{cases}, \tag{3.21}$$

where j_l is the spherical Bessel function of the first kind, and h_l^{in} (h_l^{out}) is the spherical Hankel functions first (second) kind. The wavefunctions are normalized such that $C_l = 1$. A_l and B_l are determined by the continuity of R_l and dR_l/dr at $r = R_\oplus$,

$$A_l = -\frac{k_0 j_l(k_\oplus R_\oplus)h_{l+1}^{\text{in}}(k_0 R_\oplus) - k_\oplus j_{l+1}(k_\oplus R_\oplus)h_l^{\text{in}}(k_0 R_\oplus)}{k_0 j_l(k_\oplus R_\oplus)h_{l+1}^{\text{out}}(k_0 R_\oplus) - k_\oplus j_{l+1}(k_\oplus R_\oplus)h_l^{\text{out}}(k_0 R_\oplus)}\,, \tag{3.22}$$

$$B_l = -\frac{1}{2}\frac{k_0 h_{l+1}^{\text{in}}(k_0 R_\oplus)h_l^{\text{out}}(k_0 R_\oplus) - k_0 h_l^{\text{in}}(k_0 R_\oplus)h_{l+1}^{\text{out}}(k_0 R_\oplus)}{k_0 j_l(k_\oplus R_\oplus)h_{l+1}^{\text{out}}(k_0 R_\oplus) - k_\oplus j_{l+1}(k_\oplus R_\oplus)h_l^{\text{out}}(k_0 R_\oplus)}\,. \tag{3.23}$$

We now match this to the an incoming plane wave. We expand $e^{i\vec{x}\cdot\vec{p}}$ in terms of spherical harmonics

$$e^{i\vec{x}\cdot\vec{p}} = \sum_{l=0}^{\infty} i^l(2l+1)j_l(px)P_l(\hat{x}\cdot\hat{p}) \tag{3.24}$$

$$= \sum_{l=0}^{\infty} i^l(2l+1)\frac{1}{2}[h_l^{\text{in}}(px) + h_l^{\text{out}}(px)]P_l(\hat{x}\cdot\hat{p})\,, \tag{3.25}$$

matching the incoming spherical waves in the above with the expression in 3.21 gives

$$X_{\vec{p}}(\vec{x}) = \sum_{l=0}^{\infty} i^l (2l+1) R_l(x) P_l(\hat{x} \cdot \hat{p}) \,. \tag{3.26}$$

Note that $\varphi_{\vec{v}}$ as described in section 3.3 is given by

$$\begin{aligned} \varphi_{\vec{v}}(t, \vec{x}) &= e^{-i\omega_v t} X_{\vec{p}}(\vec{x}) & (3.27) \\ &= \sum_{l=0}^{\infty} i^l (2l+1) e^{-i\omega_v t} R_l(x) P_l(\hat{x} \cdot \hat{p}) \,, & (3.28) \end{aligned}$$

where $\omega_v = \gamma m_\varphi$. Substituting this into equation 3.15 gives

$$\begin{aligned} \langle \varphi(t, \vec{x}) \varphi(t', \vec{y}) \rangle = \frac{\varphi_0^2}{2} \int \mathrm{d}^3 v \, g(\vec{v}) \Re \Bigg(& e^{-i\omega(t-t')} \sum_{l=0}^{\infty} \sum_{l'=0}^{\infty} (2l+1)(2l'+1) i^{l-l'} \\ & \times R_l(x) R_{l'}^*(y) P_l(\hat{x} \cdot \hat{v}) P_{l'}(\hat{y} \cdot \hat{v}) \Bigg) \,. \end{aligned} \tag{3.29}$$

As seen in equation 3.11 the relevant quantity is $\hat{x} \cdot \langle \varphi \vec{\nabla} \varphi \rangle$ which can be found from equation 3.29 as

$$\begin{aligned} \hat{x} \cdot \langle \varphi \vec{\nabla} \varphi \rangle = \frac{1}{2} \varphi_0^2 \int \mathrm{d}^3 v \, g(\vec{v}) \sum_{l=0}^{\infty} \sum_{l'=0}^{\infty} \Re \Bigg(& (2l+1)(2l'+1) i^{l-l'} \\ & \times R_l(x) \frac{\partial}{\partial x} R_{l'}^*(x) P_l(\hat{x} \cdot \hat{v}) P_{l'}(\hat{x} \cdot \hat{v}) \Bigg) \,. \end{aligned} \tag{3.30}$$

This expression is computationally difficult to evaluate because of the large number of 3-d integrals that need to be evaluated, one can dramatically reduce the computational resources required by replacing a realistic dark matter violation distribution with a spherically symmetric one. Doing this we can preform the angular integrals and one of the sums to get

$$\hat{x} \cdot \langle \varphi \vec{\nabla} \varphi \rangle = 2\pi \varphi_0^2 \int_0^{\infty} v^2 \mathrm{d}v \, g(v) \sum_{l=0}^{\infty} (2l+1) R_l(x) \frac{\partial}{\partial x} R_l^*(x) \,. \tag{3.31}$$

This simplification does introduce $O(1)$ errors but are the correct order of magnitude. The effect of the dark matter wind is discussed farther in section 3.5.

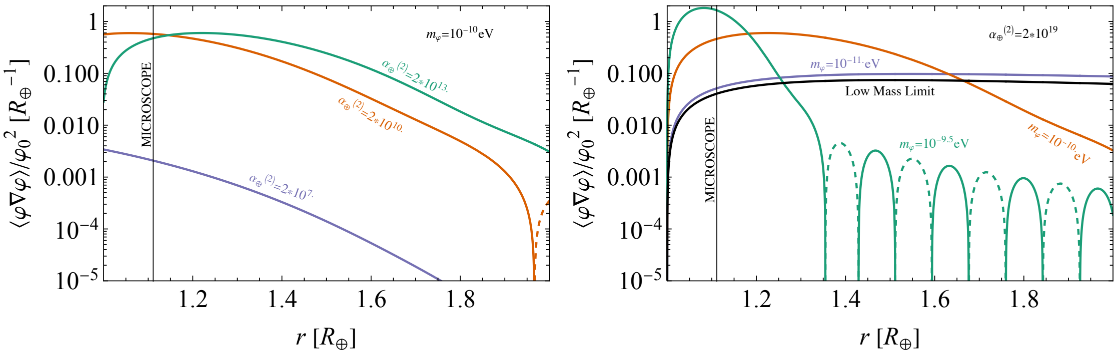

Figure 4. **Left:** Comparison of $\langle\varphi\nabla\varphi\rangle$ for fixed $m_\varphi = 10^{-10}$eV and varying d_i. **Right:** Comparison of $\langle\varphi\nabla\varphi\rangle$ for fixed d_i and $m_\varphi = 10^{-11}$eV, 10^{-10}eV, and $10^{-9.5}$eV. The homogeneous solution described in Appendix A.1 is shown in black for comparison.

The qualitative features of equation 3.31 is illustrated in figure 4. In the left panel shows $\langle\varphi\nabla\varphi\rangle$ for several different coupling strength at the same mass. For coupling such that $m^2_{\text{eff}\oplus}R_\oplus \ll 1$ the couplings are not sufficient to fully screen the φ in the Earth and so the gradient of φ is suppressed by the coupling as such in this regime $\langle\varphi\nabla\varphi\rangle$ depends linearly on the couplings.

In regime where $m^2_{\text{eff}\oplus}R_\oplus \gg 1$ the dark matter field is completely screened inside of the Earth. The screening saturates and the field goes to 0 on the surface of the Earth. Due to this, in this regime, $\langle\varphi\nabla\varphi\rangle$ does not depend on the couplings.

For high couplings the field is completely screened inside of the Earth, as such in this limit $\langle\varphi\nabla\varphi\rangle$ no longer depends on the couplings as shown in appendix A.2.1.

The right panel shows $\langle\varphi\nabla\varphi\rangle/\varphi_0^2$ for different masses for couplings in the strong coupling regime. We can see that for low masses when the typical wavelength of the dark matter is much larger that the radius of the Earth $\langle\varphi\nabla\varphi\rangle$ approaches

$$\langle\varphi\nabla\varphi\rangle \approx -\varphi_0^2\frac{A}{x^2}(1-\frac{A}{x})\,, \tag{3.32}$$

with

$$A = \frac{m_{\mathrm{ind}\oplus} R_\oplus - \tanh(m_{\mathrm{ind}\oplus} R_\oplus)}{m_{\mathrm{ind}\oplus}} \,. \tag{3.33}$$

This expression is derived from equation 3.30 in appendix A.2.2. This expression is equivalent to the findings in [29]. The derivation in [29] is summarized in appendix A.1. The intuition behind this is that when the wave length is large compared to the size of the Earth it can be treated as a oscillating homogeneous field at infinity.

When the typical wavelength is comparable or much smaller than the radius of the Earth the behavior is more complicated. This regime is only constrained in the strong coupling limit so we will focus the discussion on the high mass strong coupling regime. As seen in figure 4 in this regime as one moves away from the Earth the $\langle \varphi \nabla \varphi \rangle$ rises linearly with slope $\propto {k_0^t}^2$ with k_0^t the typical wavelength on the dark matter. At a distance from the Earth approximately equal to a quarter of the typical wavelength $\langle \varphi \nabla \varphi \rangle$ reaches a maximum. Farther away from the Earth than this $\langle \varphi \nabla \varphi \rangle$ oscillates and decays rapidly.

3.5 The dark matter wind

The dark matter velocity distribution discussed in section 3.3 is typically given by the standard halo model. In the standard halo model the dark-matter velocity distribution follows a Maxwell–Boltzmann profile in the Galactic rest frame. Because the Solar System orbits the Galactic centre, the distribution in the Earth's rest frame is a boosted Maxwell–Boltzmann distribution, with dark matter preferentially arriving from the direction of the constellation Cygnus, this incoming flux is often called the dark-matter wind.

In the preceding sections we neglected the wind to keep the evaluation of equation (3.30) computationally tractable. Although the wind is unlikely to change

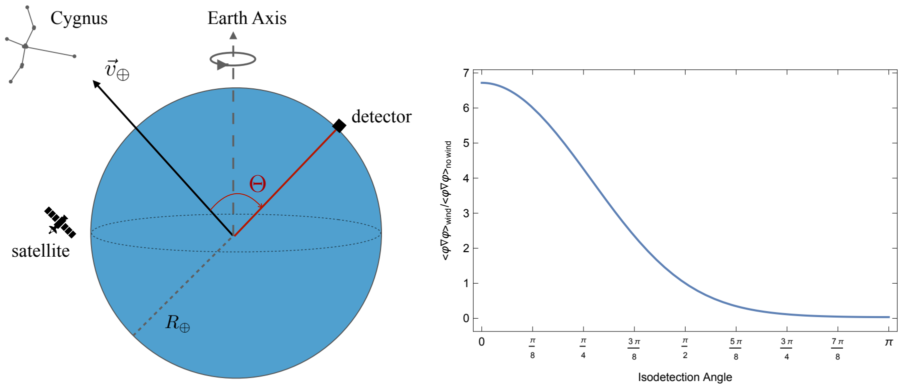

Figure 5. A plot show the modulation in a Eöt-Wash type experiment that is near the surface of the Earth.

our limits by more than an order of magnitude, or alter the qualitative behavior described in section 3.6, it is not necessarily negligible.

The principal effect arises when the typical dark-matter wavelength is much smaller than the Earth's radius: the Earth then casts a shadow. Whenever the Earth lies between the experiment and Cygnus, dark matter arriving from that direction is largely scattered away, reducing the average value of φ^2 and consequently suppressing any signal. This shadowing is less pronounced for space-based experiments, because the Earth subtends a smaller solid angle and so blocks fewer arrival directions.

The shadow effect induces a characteristic modulation as a satellite orbits the Earth: the signal varies with the isodetection angle, defined as the angle between (i) the line from the satellite to the Earth's centre and (ii) the line from the Earth's centre to Cygnus. For satellite orbits in orbit around the earth this modulation has the period of the orbit of the satellite, for an earth based experiment the period would be the sidereal day. Figure 5 illustrates this modulation for an experiment located near the Earth's surface.

3.6 Results

The constraints obtained from the MICROSCOPE experiment are shown as the magenta lines in Figure 6. For masses below $10^{-11}\,\mathrm{eV}$ the typical wavelength of the dark matter exceeds the size of the Earth, and our results reproduce the constraints reported in [29]. In this low-mass region there are two distinct scaling behaviors. For masses below $10^{-16}\,\mathrm{eV}$ MICROSCOPE is sensitive enough to probe the *weak-coupling* regime, in which the screening length is larger than the size of the Earth; here the constraint scales as $d^{(2)} \propto m_\varphi$. For $m_\varphi \gtrsim 10^{-15}\,\mathrm{eV}$ the experiment accesses only the *strong-screening* regime, where the screening length is short compared with the satellite altitude; in this band the constraint scales as $d^{(2)} \propto m_\varphi^2$. For masses between 10^{-11} and $10^{-10}\,\mathrm{eV}$ the wavelength remains larger than the size of the Earth but smaller than the satellite altitude, rendering the constraint independent of m_φ. When $m_\varphi \gtrsim 10^{-9}\,\mathrm{eV}$ the wavelength is smaller than the altitude of MICROSCOPE. In this regime the dark-matter field loses coherence, destructive interference makes the constraint oscillatory, and the envelope scales as $d^{(2)} \propto m_\varphi^3$.

The proposed *Galileo* mission is a more sensitive space-based test of the equivalence principle. If realized, it aims to bound the Eötvös parameter at the 10^{-17} level while operating at an altitude of 600 km. For comparison, MICROSCOPE measured $\eta = (-0.1 \pm 1.3) \times 10^{-14}$ at an altitude of 710 km. The projected constraints from *Galileo* are shown as the dashed blue line in Figure 6. Although the overall shape resembles that of MICROSCOPE, the transition from weak to strong screening occurs at higher mass because of *Galileo*'s greater sensitivity.

Eöt-Wash is an Earth-based laboratory test of the equivalence principle. The dotted brown line in Figure 6 depicts the constraints that could be expected from Eöt-Wash if atmospheric screening were negligible, revealing several qualitative differences from MICROSCOPE. For $m_\varphi \lesssim 10^{-16}\,\text{eV}$ Eöt-Wash, like MICROSCOPE, probes only the weak-screening regime. Between 10^{-16} and $10^{-13}\,\text{eV}$ it tests an *intermediate* regime in which the screening length is larger than the size of the Earth but smaller than the experiment's effective altitude; the constraint then scales as $d^{(2)} \propto m_\varphi^4$. From 10^{-13} to $10^{-11}\,\text{eV}$ Eöt-Wash constrains the strong-screening, low-mass region much like MICROSCOPE. Above $10^{-11}\,\text{eV}$ the constraint again becomes independent of m_φ until the wavelength drops below $\mathcal{O}(\text{m})$ which is near the scale of the apparatus and the implicit assumption made in this chapter that the experiment is point-like breaks down. To illustrate altitude dependence, the dotted black line in Figure 6 shows the constraint that would be obtained if Eöt-Wash were operated at an altitude of 4340 m. In the weak and intermediate regimes the constraint is altitude-independent, whereas in the strong-screening regime it grows linearly with altitude until the onset of oscillations. These Eöt-Wash curves are intended as qualitative illustrations only; they neglect atmospheric screening, which becomes important for couplings $d^{(2)} \gtrsim 10^{20}\,\text{eV}$.

3.7 Conclusion

In this chapter we investigated how ULDM with quadratic couplings affects searches for violations of the equivalence principle. Such experiments already set stringent limits on quadratically coupled ULDM, as shown in Ref. [29]; however, we have demonstrated that the finite velocity dispersion of the Galactic halo can substantially reshape these bounds when the DM de Broglie wavelength is comparable to the size of the Earth. Velocity dispersion *weakens* the constraints when the wavelength is much larger than the Earth, but can *strengthen* them in the intermediate regime where the wavelength is of the same order as the Earth's radius.

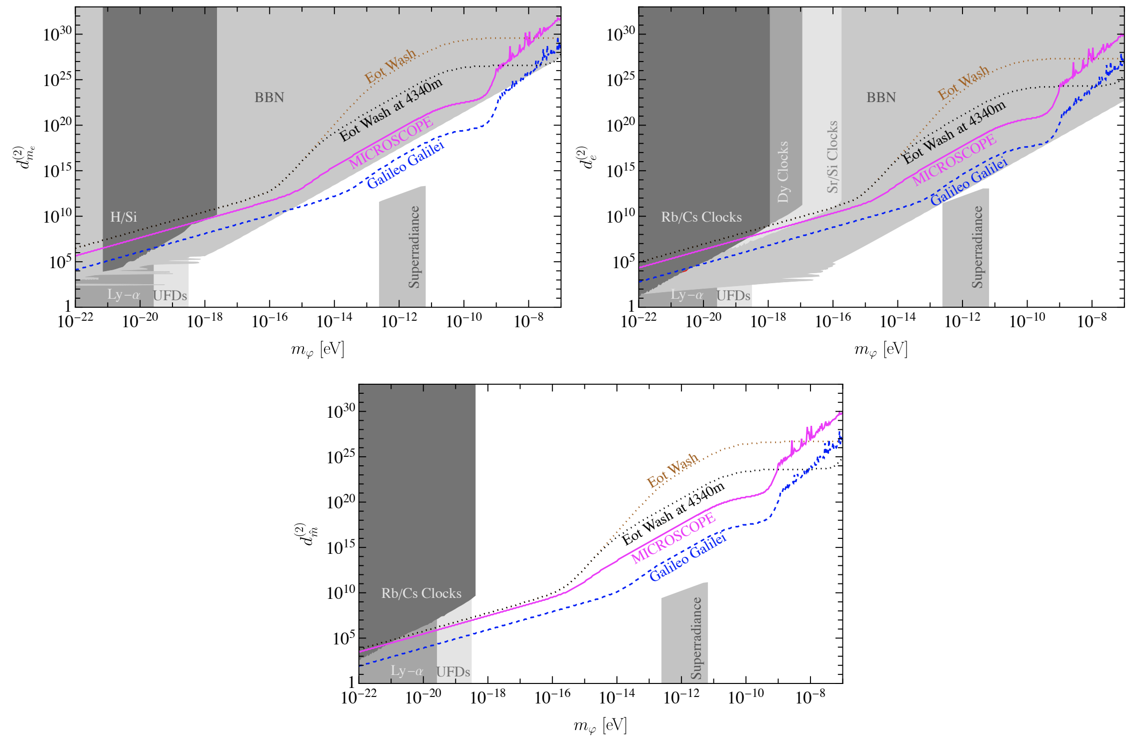

Figure 6. Constraints on quadratic couplings of ULDM to electrons, photons, and quarks. The area above the magenta lines show regions contained by the MICROSCOPE experiment as calculated in this paper. The dashed blue lines show the projected constrains from the Galileo experiment. The dotted brown and black lines are shown to illustrate the properties of the constrains form weak equivalence principle experiments near the surface of the Earth. They show respectively the Eöt-wash experiment and a hypothetical equivalence principle violation experiment with the same sensitivity as the Eöt-wash experiment but at an altitude of 4340m. In both cases ignoring screening from the atmosphere. The grey regions show parameter space ruled out by prior work from atomic clock experiments [53, 29] as well as constraints from Lyman-α [2], UFDs [3] superradiance [23, 54] and Big Bang Nucleosynthesis [36]

CHAPTER IV

SPECTROSCOPY FOR ULTRALIGHT DARK MATTER

The work presented in this chapter was carried out in collaboration with David Allcock, Gabe Gregory, Logan Page, Marcus Polk, Evan Ritchie, Natalie Velez, David Wineland, and Tien-Tien Yu.[65] Presented here are my own contributions to the project.

4.1 Introduction

Precision measurements provide sensitive probes of temporal variations in fundamental constants, both in terrestrial laboratories and in space. Among the most powerful techniques are atomic-clock comparisons: by monitoring the ratio of two independent atomic transition frequencies (which need not belong to the same species) over time, one can place stringent limits on any drift in that ratio. These limits translate into strong constraints on the couplings of ultralight dark matter (ULDM) to photons, quarks, and gluons [13, 29]. The leading clock comparisons, however, are only weakly sensitive to ULDM–electron couplings because near-cancellations suppress the relevant frequency dependence.

Time-resolved spectroscopy offers a complementary approach. By repeatedly measuring the *absolute* frequency of a single atomic or molecular transition, one can search directly for time-dependent shifts induced by varying constants. This strategy was pioneered by [66], who monitored electronic lines in iodine gas. **SP**ectroscopy for **U**ltralight **D**ark matter (SPUD) extends the idea to vibrational transitions in hydrogen cyanide (HCN). Certain HCN lines are almost purely vibrational, greatly enhancing sensitivity to couplings that modify nuclear masses, as discussed in section 4.4.

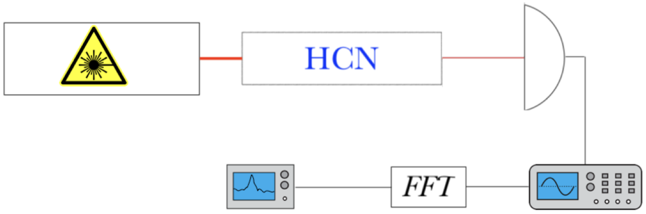

Figure 7. Conceptual schematic of the SPUD experiment.

Compared with clock-comparison experiments, time-resolved spectroscopy sacrifices sensitivity but gains orders of magnitude in temporal resolution. This enables SPUD-type experiments to probe ULDM masses higher than those currently accessible to atomic-clock searches.

4.2 SPECTROSCOPY FOR ULTRALIGHT DARK MATTER: EXPERIMENTAL SETUP

The SPUD experimental setup is conceptually straightforward, as illustrated in figure 7. A narrow-linewidth laser is tuned (or slightly detuned) to a chosen rovibrational transition of HCN, i.e. a transition between the vibrational and rotational states of HCN. The beam passes through a cell containing dilute HCN gas, and the transmitted power is recorded in real time with a fast photodiode.

Temporal variations of the fundamental constants—introduced in section 4.3 and quantified in section 4.4—shift the molecular transition frequency. As the transition drifts, the fixed-frequency laser samples the evolving line shape, producing an amplitude modulation of the transmitted light at the ultralight-dark-matter oscillation frequency. That the frequency from the laser is fixed is justified in section 4.5. This generates a spectrally narrow signal in the photodiode output that can be searched for using standard spectral-analysis techniques.

4.3 Linearly Coupled Ultralight Dark Matter

SPUD can, in principle, probe both *linearly* and *quadratically* coupled ULDM. Screening by the Earth and its atmosphere, however, greatly suppresses signals from quadratic couplings, so the experiment's reach for that model is limited. Experiments similar to SPUD have been proposed that are to be located in space, these experiments[1] would overcome this limitation and be sensitive to quadratically coupled ultralight dark matter [67]. However with SPUD currently being earth bound, we focus here on linearly coupled ULDM.

To model a linearly coupled ULDM candidate we extend the Standard Model by a real scalar field φ and add to the Lagrangian

$$\mathcal{L} \supset \frac{M_{\rm pl}^2}{8\pi}\big(\partial^\mu\varphi\,\partial_\mu\varphi - m_\varphi^2\varphi^2\big), \tag{4.1}$$

where $M_{\rm pl} = 1.22 \times 10^{19}\,\mathrm{GeV}$ is the Planck mass, m_φ is the ULDM mass, and φ is unitless and it is related to a canonically normalized scalar field ϕ by $\varphi = \frac{\sqrt{4\pi}\phi}{M_{\rm pl}}$. The linear interactions of φ with the Standard Model are parametrised by

$$\begin{aligned}\mathcal{L} \supset \varphi\Big[&\frac{d_e^{(1)}}{16\pi\alpha}\,F^{\mu\nu}F_{\mu\nu} - \frac{d_g^{(1)}\beta_3}{2g_3}\ \mathrm{tr}\big(G^{\mu\nu}G_{\mu\nu}\big)\\ &- d_{m_e}^{(1)}\,m_e\bar{e}e - \sum_{i=u,d}\big(d_{m_i}^{(1)} + \gamma_{m_i}d_g^{(1)}\big)\,m_i\bar{\psi}_i\psi_i\Big],\end{aligned} \tag{4.2}$$

where $\alpha \simeq 1/137$ is the fine-structure constant, β_3 is the QCD beta function, g_3 is the QCD gauge coupling, and γ_{m_i} denote the anomalous dimensions of the light-quark masses.

---

[1] Which we propose be called SPUDnik

With φ treated as a classical background field, the interactions in equation (4.2) induce fractional shifts in the fundamental constants:

$$\frac{\Delta\alpha}{\alpha} = d_e^{(1)}\,\varphi, \tag{4.3}$$

$$\frac{\Delta\Lambda_{\rm QCD}}{\Lambda_{\rm QCD}} = d_g^{(1)}\,\varphi, \tag{4.4}$$

$$\frac{\Delta m_f}{m_f} = d_{m_f}^{(1)}\,\varphi, \qquad (f = e, u, d, s). \tag{4.5}$$

Here $\Lambda_{\rm QCD}$ is the QCD confinement scale and m_f denotes the relevant fermion mass.

Assuming that φ constitutes all of the dark matter, the field oscillates about the minimum of its potential with angular frequency m_φ and amplitude

$$\varphi_0 = \sqrt{\frac{8\pi\rho_{\rm DM}}{M_{\rm pl}^2\,m_\varphi^2}} \;\simeq\; 7\times10^{-31}\,\frac{\rm eV}{m_\varphi}, \tag{4.6}$$

so that

$$\varphi(t) = \varphi_0\cos\bigl(m_\varphi t + \delta\bigr)\,, \tag{4.7}$$

where δ is some phase. Equations (4.3)–(4.5) together with (4.7) therefore imply that the fundamental constants vary sinusoidally at angular frequency m_φ.

The expressions above neglects finite velocity distribution of dark matter. In reality, halo dark matter is virialised and possesses a velocity dispersion, leading to a finite spectral width of order $\Delta\omega/\omega \sim 10^{-6}$. This velocity distribution broadens spectral support of the signal, as discussed in section 4.6.

4.4 EFFECT OF ULDM ON MOLECULAR SPECTROSCOPY

Temporal variations of the fundamental constants induce corresponding oscillations in molecular transition frequencies at the angular frequency m_φ. The exact response depends on the type of transition.

For a purely *electronic* transition the energy scale is set by the Rydberg energy,

$$\omega_e \;\propto\; E_{\rm Ry} \;=\; \tfrac{1}{2}\,m_e\alpha^2. \tag{4.8}$$

For a *vibrational* transition in a diatomic molecule,

$$\omega_{\text{vib}} \;\propto\; E_{\text{Ry}}\sqrt{\frac{m_e}{\mu}}, \tag{4.9}$$

where $\mu \equiv m_A m_B/(m_A + m_B)$ is the reduced nuclear mass.

For a *rotational* transition,

$$\omega_{\text{rot}} \;\propto\; E_{\text{Ry}}\,\frac{m_e}{\mu}. \tag{4.10}$$

Applying equations (4.3) and (4.5) to equation (4.9) yields

$$\begin{aligned}\frac{\Delta\omega_{\text{vib}}}{\omega_{\text{vib}}} &= 2\,\frac{\Delta\alpha}{\alpha} + \tfrac{3}{2}\,\frac{\Delta m_e}{m_e} - \tfrac{1}{2}\,\frac{\Delta\mu}{\mu} \\ &= 2\,\frac{\Delta\alpha}{\alpha} + \tfrac{3}{2}\,\frac{\Delta m_e}{m_e} - \tfrac{1}{2}\Big(\frac{\mu}{m_A}\frac{\Delta m_A}{m_A} + \frac{\mu}{m_B}\frac{\Delta m_B}{m_B}\Big), \end{aligned}\tag{4.11}$$

where m_A and m_B are the nuclear masses. The dependence of $m_{A,B}$ on the fundamental constants (and therefore on the ULDM field) is mass- and atomic-number dependent; see Ref. [8] for a detailed discussion and derivation of the dependance of m_A and m_B on fundamental constants

4.4.1 Non-relativistic Hamiltonian

To motivate the scalings in equations (4.8) to (4.10), we can neglect relativistic and spin–spin effects and write the non-relativistic Hamiltonian for a diatomic molecule as

$$H = \frac{\mathbf{p}_A^2}{2m_A} + \frac{\mathbf{p}_B^2}{2m_B} + \sum_a \frac{\mathbf{p}_a^2}{2m_e} + \sum_{a<b}\frac{\alpha}{|\mathbf{r}_a - \mathbf{r}_b|} - \sum_{a,A}\frac{\alpha Z_A}{|\mathbf{r}_a - \mathbf{R}_A|} + \frac{\alpha Z_A Z_B}{|\mathbf{R}_A - \mathbf{R}_B|}, \tag{4.12}$$

where capital indices A, B label the nuclei and lower-case indices label the electrons. By separating electronic, vibrational, and rotational contributions and scaling coordinates we can reproduce the energy dependences quoted above.

We factor out the Rydberg energy $E_{\mathrm{Ry}} = \frac{1}{2}\,\alpha^2 m_e$ and the Bohr radius $a_0 = 1/(\alpha m_e)$ to rewrite the full Hamiltonian as

$$\begin{aligned} H \;=\; E_{\mathrm{Ry}} \Bigg[& \frac{m_e}{m_A}\big(\mathbf{p}_A a_0\big)^2 + \frac{m_e}{m_B}\big(\mathbf{p}_B a_0\big)^2 + \sum_a \big(\mathbf{p}_a a_0\big)^2 \\ & + \sum_{a<b} \frac{1}{|\mathbf{r}_a/a_0 - \mathbf{r}_b/a_0|} - \sum_{a,A} \frac{Z_A}{|\mathbf{r}_a/a_0 - \mathbf{R}_A/a_0|} + \frac{Z_A Z_B}{|\mathbf{R}_A/a_0 - \mathbf{R}_B/a_0|} \Bigg], \end{aligned} \tag{4.13}$$

where capital Roman indices label nuclei and lower-case indices label electrons.

Within the Born–Oppenheimer approximation the electronic Hamiltonian for fixed nuclear separation becomes

$$H_e = E_{\mathrm{Ry}} \left[\sum_a \big(\mathbf{p}_a a_0\big)^2 + \sum_{a<b} \frac{1}{|\mathbf{r}_a/a_0 - \mathbf{r}_b/a_0|} - \sum_{a,A} \frac{Z_A}{|\mathbf{r}_a/a_0 - \mathbf{R}_A/a_0|} + \frac{Z_A Z_B}{|\mathbf{R}_A/a_0 - \mathbf{R}_B/a_0|} \right]. \tag{4.14}$$

Because H_e/E_{Ry} is dimensionless and its dependence on fundamental constants enters only through the scale a_0^{-1}, its eigenvalues can be written $E_i(r_A, r_B) = E_{\mathrm{Ry}}\, u_i\big(|\mathbf{R}_A - \mathbf{R}_B|/a_0\big)$, with the dimensionless functions u_i independent of α and m_e. Hence a purely electronic transition obeys $\omega_e \propto E_{\mathrm{Ry}}$, confirming equation (4.8).

Introducing the centre-of-mass momentum $\mathbf{P} = \mathbf{p}_A + \mathbf{p}_B$, the relative coordinate $r = |\mathbf{R}_A - \mathbf{R}_B|$, the reduced mass $\mu = m_A m_B/(m_A + m_B)$, and the total mass $M = m_A + m_B$, the nuclear Hamiltonian becomes

$$H_N = E_{\mathrm{Ry}} \left[\frac{m_e}{M}\big(\mathbf{P} a_0\big)^2 + \frac{m_e}{\mu}\big(p_r a_0\big)^2 + \frac{m_e a_0^2 L^2}{\mu r^2} + u_i(r/a_0) \right], \tag{4.15}$$

where p_r is the momentum conjugate to r and L is the orbital angular momentum.

Near equilibrium we approximate $u_i(r/a_0) \simeq \kappa\,(r/a_0 - q_0)^2$, with dimensionless constants κ and q_0 that are again independent of α and m_e. In the centre-of-mass frame this gives

$$H_N = E_{\mathrm{Ry}} \left[\frac{m_e}{\mu}\big(p_r a_0\big)^2 + \frac{m_e a_0^2 L^2}{\mu r^2} + \kappa\,(r/a_0 - q_0)^2 \right]. \tag{4.16}$$

The harmonic-oscillator frequency is

$$\omega_{\rm vib} \;=\; E_{\rm Ry}\sqrt{\kappa\,\frac{m_e}{\mu}} \;\propto\; E_{\rm Ry}\sqrt{\frac{m_e}{\mu}}, \tag{4.17}$$

reproducing equation (4.9). The spatial width of a vibrational state is

$$\frac{1}{\sqrt{m_{\rm eff}\omega_{\rm vib}}} = a_0\big(m_e/\mu\kappa\big)^{1/4} \ll a_0 \sim q_0 a_0, \tag{4.18}$$

this implies that the radial wave function is supported away from $r = 0$ so vibrational and rotational modes decouple. Writing the vibrational and rotational Hamiltonians separately,

$$H_{\rm vib} = E_{\rm Ry}\left[\frac{m_e}{\mu}\big(p_r a_0\big)^2 + \kappa\,(r/a_0 - q_0)^2\right], \tag{4.19}$$

$$H_{\rm rot} = E_{\rm Ry}\left[\frac{m_e L^2}{\mu q_0}\right], \tag{4.20}$$

one finds $\omega_{\rm rot} \propto E_{\rm Ry}\, m_e/\mu$, confirming equation (4.10).

For general polyatomic molecules rovibrational structure is considerably more complex [68, 69]. Nevertheless the α- and m_e-dependence of ω_e, $\omega_{\rm rot}$, and $\omega_{\rm vib}$ is expected to follow the same scaling as in the diatomic case; the principal difference is that each normal mode has a distinct dependence on the individual nuclear masses. For the linear molecule hydrogen cyanide used in SPUD, the normal modes are tabulated in Ref. [70] and can be employed to evaluate the mass dependence of $\omega_{\rm vib}$ precisely. Using those results for the specific vibrational line employed by SPUD one obtains

$$\begin{aligned}\frac{\Delta\omega_{\rm vib}}{\omega_{\rm vib}} &= 2\,\frac{\Delta\alpha}{\alpha} + \tfrac{3}{2}\,\frac{\Delta m_e}{m_e} - \tfrac{1}{2}\,\frac{\Delta\mu_{\rm eff}}{\mu_{\rm eff}} \\ &\approx 2\,\frac{\Delta\alpha}{\alpha} + \tfrac{3}{2}\,\frac{\Delta m_e}{m_e} - \tfrac{1}{2}\Big(0.94\,\frac{\Delta m_{\rm H}}{m_{\rm H}} + 6\times10^{-4}\,\frac{\Delta m_{\rm C}}{m_{\rm C}} + 0.06\,\frac{\Delta m_{\rm N}}{m_{\rm N}}\Big),\end{aligned} \tag{4.21}$$

where $m_{\rm H}$, $m_{\rm C}$, and $m_{\rm N}$ denote the masses of ^{1}H, ^{12}C, and ^{14}N, respectively. Combining this relation with Eqs. (3.6)–(3.3) of Ref. [28], the strange quark contribution from [71], and with Eqs. (4.3)–(4.5) yields

$$\frac{\Delta\omega_{\rm vib}}{\omega_{\rm vib}} \approx -0.46\,\frac{\Delta\Lambda_{\rm QCD}}{\Lambda_{\rm QCD}} - 0.02\,\frac{\Delta\hat{m}}{\hat{m}} + 8\times10^{-4}\,\frac{\Delta\delta m}{\delta m} - 0.02\,\frac{\Delta m_s}{m_s} + 1.5\,\frac{\Delta m_e}{m_e} + 2\,\frac{\Delta\alpha}{\alpha} \tag{4.22}$$

$$= \varphi\Big(-0.46\,d_g^{(1)} - 0.02\,d_{\hat{m}}^{(1)} + 8\times10^{-4}\,d_{\delta m}^{(1)} - 0.02\,d_{m_s}^{(1)} + 1.5\,d_{m_e}^{(1)} + 2\,d_e^{(1)}\Big)\,. \tag{4.23}$$

The SPUD experimental setup described in section 4.2 measures $\Delta\omega_{\rm vib}/\omega_{\rm vib}$; the expression above then translates the observation directly into constraints on the ULDM couplings $d_i^{(1)}$.

We can compare equation (4.23) to dependance of the the specific transition of I_2 used in experiment B of [66] on φ given below

$$\frac{\Delta\omega_{\rm I_2}}{\omega_{\rm I_2}} = \varphi\Big(-0.06\,d_g^{(1)} - 0.006\,d_{\hat{m}}^{(1)} + 2\times10^{-5}\,d_{\delta m}^{(1)} - 0.003\,d_{m_s}^{(1)} + 0.93\,d_{m_e}^{(1)} + 2\,d_e^{(1)}\Big)\,. \tag{4.24}$$

Note that because that transition was mostly electronic and only slightly vibrational the dependance on nuclear couplings is smaller than the nearly purely vibrational transition used for SPUD.

4.5 Effect of ULDM on Laser

In the foregoing analysis we treated the laser frequency as fixed, a point that deserves clarification. The laser frequency is set by the physical length of its optical cavity, which may be viewed as an assembly of atoms. Because atomic dimensions scale with the Bohr radius, the cavity length obeys $L_{\rm Laser} \propto a_0 = (\alpha m_e)^{-1}$. However, as long as the ULDM oscillation frequency exceeds the lowest mechanical (vibrational) modes of the cavity, the cavity behaves as a rigid body owing to its large acoustic impedance at those frequencies [72]. This condition holds throughout the dark-matter mass range probed by SPUD, justifying our assumption of a constant laser frequency.

4.6 Accounting for DM decoherence

The foregoing discussion ignores the finite velocity dispersion of the dark-matter halo. Because the field is not perfectly at rest, it does not oscillate at a single frequency. Within the Standard Halo Model the frequency distribution is described by the frequency distribution [73, 61]

$$f_{\mathrm{DM}}(\omega) = \frac{2}{\sqrt{\pi}\, v_0 v_E m_\varphi} \exp\Big[-\frac{2}{v_0^2}\frac{\omega - m_\varphi}{m_\varphi} - \frac{v_E^2}{v_0^2}\Big] \sinh\Big[\frac{2\sqrt{2}\, v_E}{v_0^2}\sqrt{\frac{\omega - m_\varphi}{m_\varphi}}\Big], \qquad (4.25)$$

where ω is the angular frequency of the field, $v_0 \simeq 10^{-3}c$ is the local circular speed at the Sun's galactocentric radius, and v_E is the Earth's speed in the Galactic rest frame. This implies that equation (4.7) is not exactly correct and instead $\varphi(t)$ is a random variable as described in section 3.3. This is relevant for SPUD because it leads to the signal from the photodiode would having a finite spectral support.

4.7 Conclusions

This chapter has summarized the theoretical framework underlying SPUD. The SPUD experiment is currently being assembled and commissioned as a demonstrator, laying the groundwork for a future full-scale experiment. Ultimately, SPUD is expected to be competitive with experiment B in [66], with the potential to probe larger dark matter masses due to improvements in both the experimental setup and data analysis.

CHAPTER V

CONCLUSIONS

5.1 Other Constraints

Scalar ULDM with the couplings discussed in this paper is subject to several constraints in addition to the BBN bound and equivalence principle violation constraints discussed above. This includes atomic clock experiments directly looking for varying fundamental constants, probes of cosmological structure formation, and astrophysical constraints.

5.1.1 Experiments Looking for Varying Fundamental Constants

Precision measurements can search for temporal variation in fundamental constants in labs on Earth and in space. By examining the stability of different atomic frequency standards relative to each other, tight constraints can be put on the temporal variation in the ratios of different atomic transitions (not necessarily of the same species). This puts strong constraints on the coupling of ULDM to photons, quarks and gluons [13, 29]. The most sensitive clock experiments are not sensitive to the electron coupling due to approximate cancellations for the frequency comparisons they make. Future improvements in this field may come from the development of nuclear clocks based on the nuclear transition between the ground state and the first excited state of the ^{229}Th isotope. High precision frequency comparison of the nuclear clock transition in ^{229}Th and the atomic clock transition in ^{87}Sr have all ready been made [74]. This is the a major step towards a nuclear clock that could improve on the current constraints by many orders of magnitude [57].

Matter-wave interferometry experiments are very sensitive to potential time variation in atomic transition energy [75]. A large number of upcoming experiments will probe interesting parameter space. A recent summary of progress in this field can be found in [57]. Among the most sensitive of such atom interferometers are the Earth-based AION [55] and the space-based AEDGE [56]. The Earth-based experiment is hampered by the screening effects discussed in the previous section. These experiments are also sensitive to the electron and photon couplings.

5.1.2 Structure Formation

Cosmological structures cannot form on length scales smaller than the de Broglie wavelength of the DM. To correctly reproduce structure formation, the DM must therefore be sufficiently heavy. Observations of dwarf Milky Way satellites require $m_\phi \gtrsim 3 \times 10^{-21}$ eV [76, 77, 78]. Similar constraints come from measurements of the subhalo mass function and observations of stellar streams [79, 80]. The large de Broglie wavelength also delays structure formation compared to standard cosmology, so complementary constraints arise from observations of small-scale structure at high redshift. For example, the Lyman-α forest flux power spectrum requires $m_\phi \gtrsim 2 \times 10^{-20}$ eV [2].

The strongest lower bound on the mass of ULDM comes from observations of ultra-faint dwarf galaxies (UFDs). The wave-like properties of ULDM cause DM density fluctuations that transfer energy to stars through gravitational interactions leading to dynamical heating of dwarf galaxies. Measurements of the velocity dispersion of the UFDs Segue 1 and Segue 2 require $m_\phi \gtrsim 3 \times 10^{-19}$eV [3]. Similar constraints were claimed from observation of the dwarf galaxy Eridanus II [81]. However, that analysis made strong assumptions about the solitonic core of the DM halo of Eridanus II, which were relaxed in a more detailed analysis [82].

5.1.3 Astrophysics

Astrophysical probes are also sensitive to the presence of interacting ULDM. In particular, pulsar timing arrays can be used to constrain very light ULDM in a manner complementary to the structure formation arguments discussed above [24, 25]. These constraints are weaker than the constraints from structure formation and are thus not shown here. At higher masses, constraints arise from superradiance. Bosonic radiation incident on a rotating black hole can be amplified through a process called black hole superradiance in which energy and angular momentum are extracted from the black hole in a manner similar to the Penrose process [83] and results in the spin-down of black holes [84]. The observation of old, rapidly rotating black holes can therefore be used to rule out the existence of light bosons [85, 17, 86, 18, 19, 20, 21, 22]. Observations of solar mass black holes can be used to constrain light scalars with masses in the interval $[2.7 \times 10^{-13}, 6.1 \times 10^{-12}]$ eV [23]. Supermassive black holes can also be used to constrain DM mass in the interval $[2.9 \times 10^{-21}, 1.6 \times 10^{-17}]$ eV [87, 86, 20, 54], although the spin measurements are not as robust as for solar mass black holes and less is understood about the accretion disks, whose properties may disrupt the superradiance process [84, 88]. Quadratically coupled ULDM will get an effective mass from interaction with the accretion disk in the vicinity of a black hole, potentially modifying the dynamics of superradiance. In the absence of a detailed analysis of this effect, we restrict the superradiance constraints to couplings where the induced mass from the accretion disk is subdominant to the bare mass,

$$m^2_{\text{induced}} = d_i^{(2)} \frac{2\pi}{M^2_{\text{Pl}}} 2 Q_i \rho_{\text{BH}} \ll m^2_\phi \,, \tag{5.1}$$

where ρ_{BH} is the density of the accretion disc at the radius of the boson cloud, and Q_i is the dilatonic charge of the accretion disk as in [29]. Furthermore, we neglect any self-interactions. Such self-interactions can disrupt superradiance, potentially weakening the bound further [89, 90, 23].

5.2 CONCLUSIONS

Ultralight dark matter is amenable to a wide array of complementary search strategies that probe its parameter space. Dark-matter masses below $3 \times 10^{-21}\,\mathrm{eV}$ are ruled out by observations of Milky-Way satellite galaxies, independent of any coupling to the Standard Model.

Above that mass, the most stringent limits on the couplings of ULDM to gluons, photons, electrons, and the anti-symmetric combination of quarks are the Big-Bang-Nucleosynthesis (BBN) bounds derived in **Chapter II**. In this same mass range, the leading constraints on the symmetric quark combination arise from the equivalence-principle test performed by the *MICROSCOPE* satellite, discussed in **Chapter III**. Although this constraint is weaker than—but complementary to—the BBN bounds on the other couplings, forthcoming space-based experiments such as *Galileo* could supersede the current limits.

For dark-matter masses in the interval 2.9×10^{-21}–$1.6 \times 10^{-17}\,\mathrm{eV}$, black-hole superradiance provides a *lower bound* on the allowed couplings. Combined with the upper bound from BBN, these limits exclude quadratically-coupled ULDM that interacts solely through the anti-symmetric quark operator throughout this interval. If additional quadratic couplings are present, ULDM may remain viable only within the narrow region bounded from below by superradiance and from above by the BBN or equivalence-principle constraints.

APPENDIX

APPENDICES TO **Chapter III** ON UPDATING EQUIVALENCE PRINCIPLE TEST OF ULTRALIGHT DARK MATTER

A.1 Homogeneous solution

In this appendix we reproduce the calculation done in Ref. [29] on the effect of quadratically coupled ULDM on equivalence principle violation experiments. As in Ref. [29] we assume that φ approaches a homogeneous solution as $|\vec{x}| \to \infty$; consequently the X from equation (3.18) must tend to a constant at large $|\vec{x}|$. This is possible only if $k_0 = 0$, and it further requires X to depend solely on $r = |\vec{x}|$. Under these conditions equation (3.18) reduces to

$$\frac{1}{r^2}\partial_r\big(r^2\partial_r X\big) - m_{\mathrm{eff},\oplus}^2\,\theta(R_\oplus - r)\,X = 0\,, \tag{A.1}$$

where $m_{\mathrm{eff},\oplus}^2 \equiv m_\phi^2 + m_{\mathrm{ind},\oplus}^2$ with $m_{\mathrm{ind},\oplus}^2 = \alpha_\oplus^{(2)}\,4\pi G\rho_\oplus = \alpha_\oplus^{(2)}\dfrac{3GM_\oplus}{R_\oplus^3}$. Solving (A.1) yields

$$X(r) = \begin{cases} 1 - \dfrac{A}{r}\,, & r > R_\oplus\,,\\[2ex] B\,\dfrac{\sinh\big(m_{\mathrm{eff},\oplus} r\big)}{r}\,, & r < R_\oplus\,. \end{cases} \tag{A.2}$$

Continuity of X and $\partial_r X$ at $r = R_\oplus$ fixes

$$A = \frac{m_{\mathrm{eff},\oplus}R_\oplus - \tanh(m_{\mathrm{eff},\oplus}R_\oplus)}{m_{\mathrm{eff},\oplus}}\,, \tag{A.3}$$

$$B = \frac{\mathrm{sech}(m_{\mathrm{eff},\oplus}R_\oplus)}{m_{\mathrm{eff},\oplus}}\,. \tag{A.4}$$

Substituting this solution into equation (3.11) gives

$$\eta = 2\frac{|\vec{a}_A - \vec{a}_B|}{|\vec{a}_A + \vec{a}_B|} = s_C^{(2)}\,\Delta\bar{\alpha}^{(2)}\,\frac{\varphi_0^2}{2}\Big(1 - s_C^{(2)}\frac{GM_C}{c^2 r}\Big), \tag{A.5}$$

where the effective scalar charge is

$$s_C^{(2)} = \tilde{\alpha}_C^{(2)}\,J_{\mathrm{sgn}[\tilde{\alpha}_C^{(2)}]}\left(\sqrt{2\left|\tilde{\alpha}_C^{(2)}\,\frac{GM_C}{c^2 R_C}\right|}\right), \tag{A.6}$$

with

$$J_+(z) = 3\frac{z - \tanh z}{z^3}\,, \tag{A.7}$$

$$J_-(z) = 3\frac{\tan z - z}{z^3}\,. \tag{A.8}$$

Equation (A.5) reproduces the result of Ref. [29].

The derivation above assumes that φ tends to a homogeneous value far from the Earth. As discussed in section 3.3, however, φ constitutes the Milky Way's dark-matter halo and therefore possesses a distribution of orbital velocities relative to the Earth. While it is reasonable to treat φ as spatially homogeneous *on average* over many coherence times, the field is not strictly homogeneous at any given instant—even in the absence of terrestrial screening. Nevertheless, in the long-wavelength (low-mass) limit the expression in equation (A.5) remains valid, as shown explicitly in section A.2.2.

A.2 SIMPLIFYING LIMITS

A.2.1 Strong-coupling

In this appendix we show that if $m_{\mathrm{ind}\oplus}R_\oplus \gg 1$ and $m_{\mathrm{ind}\oplus} \gg m_\varphi v_{\mathrm{esc}}$ then that dark matter is almost completely screened from the earth and $\langle\varphi\vec{\nabla}\varphi\rangle$ is independent of the coupling. The only dependence of $\langle\varphi\vec{\nabla}\varphi\rangle$ comes from A_l. Rearranging equation 3.22 gives

$$A_l = -\frac{k_0 R_\oplus h^{\mathrm{in}}_{l+1}(k_0R_\oplus) - k_\oplus R_\oplus \frac{j_{l+1}(k_\oplus R_\oplus)}{j_l(k_\oplus R_\oplus)} h^{\mathrm{in}}_l(k_0R_\oplus)}{k_0 R_\oplus h^{\mathrm{out}}_{l+1}(k_0R_\oplus) - k_\oplus R_\oplus \frac{j_{l+1}(k_\oplus R_\oplus)}{j_l(k_\oplus R_\oplus)} h^{\mathrm{out}}_l(k_0R_\oplus)}\,, \tag{A.9}$$

Now note that in this regime $k_\oplus R_\oplus = \sqrt{k_0^2 - m^2_{\mathrm{ind}\oplus}}R_\oplus \approx i m_{\mathrm{ind}\oplus}R_\oplus$. And so

$$j_l(k_\oplus R_\oplus) \approx j_l(i m_{\mathrm{ind}\oplus}R_\oplus) \tag{A.10}$$

$$\approx \frac{i^l}{2}\frac{e^{m_{\mathrm{ind}\oplus}}}{m_{\mathrm{ind}\oplus}R_\oplus}\left(1 - \frac{l(l+1)}{m_{\mathrm{ind}\oplus}R_\oplus}\right) \tag{A.11}$$

Therefore

$$\frac{j_{l+1}(k_\oplus R_\oplus)}{j_l(k_\oplus R_\oplus)} \approx i\left(1 - \frac{l+1}{m_{\mathrm{ind}\oplus} R_\oplus}\right) \tag{A.12}$$

plugging this into equation A.9 gives

$$A_l = -\frac{h_l^{\mathrm{in}}(k_0 R_\oplus)}{h_l^{\mathrm{out}}(k_0 R_\oplus)} + O\left(\frac{1}{m_{\mathrm{ind}\oplus} R_\oplus}\right) \tag{A.13}$$

So for sufficiently large coupling A_l and therefore $\langle \varphi \vec{\nabla} \varphi \rangle$ are approximately independent of the coupling.

A.2.2 Low-mass

In this appendix we show that if $m_\varphi v_{\mathrm{esc}} R_\oplus < m_\varphi v_{\mathrm{esc}} r \ll 1$ then the wavelength of the dark matter is much longer than the size of the earth and the distance to MICROSCOPE so appears to approach a homogeneous solution far from the earth. In this regime the homogeneous solution calculation is valid. This can be derived from the full calculation as follows. Rewriting

$$A_l - 1 = -\frac{k_0 R_\oplus \left(h_{l+1}^{\mathrm{in}}(k_0 R_\oplus) + h_{l+1}^{\mathrm{out}}(k_0 R_\oplus)\right) - k_\oplus R_\oplus \beta_l \left(h_l^{\mathrm{in}}(k_0 R_\oplus) + h_l^{\mathrm{out}}(k_0 R_\oplus)\right)}{k_0 R_\oplus h_{l+1}^{\mathrm{out}}(k_0 R_\oplus) - k_\oplus R_\oplus \beta_l h_l^{\mathrm{out}}(k_0 R_\oplus)} \tag{A.14}$$

$$= -2\frac{k_0 R_\oplus j_{l+1}(k_0 R_\oplus) - k_\oplus R_\oplus \beta_l j_l(k_0 R_\oplus)}{k_0 R_\oplus h_{l+1}^{\mathrm{out}}(k_0 R_\oplus) - k_\oplus R_\oplus \beta_l h_l^{\mathrm{out}}(k_0 R_\oplus)} \tag{A.15}$$

$$\approx 2\frac{k_\oplus R_\oplus \beta_l \frac{(k_0 R_\oplus)^l}{(2l+1)!!}}{k_0 R_\oplus i \frac{(2l+1)!!}{(k_0 R_\oplus)^{l+2}} - k_\oplus R_\oplus \beta_l i \frac{(2l-1)!!}{(k_0 R_\oplus)^{l+1}}}\,, \tag{A.16}$$

$$= -2i\frac{\left((k_0 R_\oplus\right)^{2l+1}}{((2l+1)!!)^2}\frac{k_\oplus R_\oplus \beta_l}{1 - k_\oplus R_\oplus \beta_l/(2l+1)}\,, \tag{A.17}$$

$$\approx 2\frac{\left((k_0 R_\oplus\right)^{2l+1}}{((2l+1)!!)^2}\frac{m_{\mathrm{ind}\oplus} R_\oplus \beta_l}{1 - i m_{\mathrm{ind}\oplus} R_\oplus \beta_l/(2l+1)}\,, \tag{A.18}$$

$$= O(\left(k_0 R_\oplus\right)^{2l+1}) \tag{A.19}$$

with $\beta_l = \frac{j_{l+1}(k_\oplus R_\oplus)}{j_l(k_\oplus R_\oplus)}$. Having used

$$j_l(z) \approx \frac{z^l}{(2l+1)!!}\,, \tag{A.20}$$

$$h_l^{\text{out}}(z) \approx i\frac{(2l-1)!!}{z^{l+1}}\,, \tag{A.21}$$

Inserting into equation 3.21 gives

$$R_l = \frac{1}{2}(h_l^{\text{in}}(k_0 r) + A_l h_l^{\text{out}}(k_0 r)) \tag{A.22}$$

$$= j_l(k_0 r) + \frac{1}{2}(A_l - 1)h_l^{\text{out}}(k_0 r) \tag{A.23}$$

$$= O((k_0 r)^l) + O((k_0 R_\oplus)^{2l+1})O((k_0 r)^{-l-1}) \tag{A.24}$$

$$= O((k_0 r)^l)\,, \tag{A.25}$$

Therefor at leading order only the $l = 0$ term contributes to equation 3.26

$$X_{k_0}(\vec{x}) = 4\pi \sum_{l=0}^{\infty} \sum_{m=-l}^{l} i^l R_l(r) Y_l^m(\hat{x}) Y^{*m}_{\;l}(\hat{p}) \tag{A.26}$$

$$= R_0(r) + O(k_0 r) \tag{A.27}$$

$$= j_0(k_0 r) + \frac{1}{2}(A_0 - 1)h_0^{\text{out}}(k_0 r) + O(k_0 r) \tag{A.28}$$

$$= 1 + \frac{1}{2}\left(2k_0 R_\oplus \frac{m_{\text{ind}\oplus} R_\oplus \beta_0}{1 - i m_{\text{ind}\oplus} R_\oplus \beta_0}\right)\frac{i}{k_0 r} \tag{A.29}$$

$$= 1 + \frac{i m_{\text{ind}\oplus} R_\oplus \beta_0}{1 - i m_{\text{ind}\oplus} R_\oplus \beta_0}\frac{R_\oplus}{r} \tag{A.30}$$

$$. \tag{A.31}$$

writing $|x| = r$. Note that

$$z\frac{j_1(z)}{j_0(z)} = z\frac{\frac{\sin(z) - z\cos(z)}{z^2}}{\frac{\sin(z)}{z}} = 1 - z\cot(z)\,, \tag{A.32}$$

so

$$i m_{\text{ind}\oplus} R_\oplus \beta_0 = 1 - m_{\text{ind}\oplus} R_\oplus \coth(m_{\text{ind}\oplus} R_\oplus)\,, \tag{A.33}$$

so

$$X_{k_0} = 1 + \frac{1 - m_{\mathrm{ind}\oplus} R_\oplus \coth(m_{\mathrm{ind}\oplus} R_\oplus)}{m_{\mathrm{ind}\oplus} R_\oplus \coth(m_{\mathrm{ind}\oplus} R_\oplus)} \frac{R_\oplus}{r} \tag{A.34}$$

$$= 1 - \frac{m_{\mathrm{ind}\oplus} R_\oplus - \tanh(m_{\mathrm{ind}\oplus} R_\oplus)}{m_{\mathrm{ind}\oplus}} \frac{1}{r} \tag{A.35}$$

$$= 1 - \frac{A}{r}\,, \tag{A.36}$$

which the same as equation A.2 from section A.1. Therefor the dark matter wave function and consequently the Eötvos are as given by the homogeneous calculation.

REFERENCES CITED

[1] Particle Data Group collaboration, *Review of Particle Physics*, *PTEP* **2022** (2022) 083C01.

[2] K.K. Rogers and H.V. Peiris, *Strong Bound on Canonical Ultralight Axion Dark Matter from the Lyman-Alpha Forest*, *Phys. Rev. Lett.* **126** (2021) 071302 [`2007.12705`].

[3] N. Dalal and A. Kravtsov, *Excluding fuzzy dark matter with sizes and stellar kinematics of ultrafaint dwarf galaxies*, *Phys. Rev. D* **106** (2022) 063517 [`2203.05750`].

[4] J. Preskill, M.B. Wise and F. Wilczek, *Cosmology of the Invisible Axion*, *Phys. Lett. B* **120** (1983) 127.

[5] L.F. Abbott and P. Sikivie, *A Cosmological Bound on the Invisible Axion*, *Phys. Lett. B* **120** (1983) 133.

[6] M. Dine and W. Fischler, *The Not So Harmless Axion*, *Phys. Lett. B* **120** (1983) 137.

[7] T. Damour and A.M. Polyakov, *The String dilaton and a least coupling principle*, *Nucl. Phys. B* **423** (1994) 532 [`hep-th/9401069`].

[8] T. Damour and J.F. Donoghue, *Equivalence Principle Violations and Couplings of a Light Dilaton*, *Phys. Rev. D* **82** (2010) 084033 [`1007.2792`].

[9] S. Schlamminger, K.Y. Choi, T.A. Wagner, J.H. Gundlach and E.G. Adelberger, *Test of the equivalence principle using a rotating torsion balance*, *Phys. Rev. Lett.* **100** (2008) 041101 [`0712.0607`].

[10] J.G. Lee, E.G. Adelberger, T.S. Cook, S.M. Fleischer and B.R. Heckel, *New Test of the Gravitational $1/r^2$ Law at Separations down to 52 μm*, *Phys. Rev. Lett.* **124** (2020) 101101 [`2002.11761`].

[11] W.-H. Tan, A.-B. Du, W.-C. Dong, S.-Q. Yang, C.-G. Shao, S.-G. Guan et al., *Improvement for testing the gravitational inverse-square law at the submillimeter range*, *Phys. Rev. Lett.* **124** (2020) 051301.

[12] Y.-J. Chen, W.K. Tham, D.E. Krause, D. López, E. Fischbach and R.S. Decca, *Stronger limits on hypothetical yukawa interactions in the 30–8000 nm range*, *Phys. Rev. Lett.* **116** (2016) 221102.

[13] A. Arvanitaki, J. Huang and K. Van Tilburg, *Searching for dilaton dark matter with atomic clocks*, *Phys. Rev. D* **91** (2015) 015015 [`1405.2925`].

[14] LIGO Scientific, Virgo, KAGRA collaboration, *Constraints on dark photon dark matter using data from LIGO's and Virgo's third observing run*, `2105.13085`.

[15] G. Raffelt and D. Seckel, *Bounds on Exotic Particle Interactions from SN 1987a*, *Phys. Rev. Lett.* **60** (1988) 1793.

[16] K.A. Olive and M. Pospelov, *Environmental dependence of masses and coupling constants*, *Phys. Rev. D* **77** (2008) 043524 [`0709.3825`].

[17] A. Arvanitaki and S. Dubovsky, *Exploring the String Axiverse with Precision Black Hole Physics*, *Phys. Rev. D* **83** (2011) 044026 [`1004.3558`].

[18] R. Brito, V. Cardoso and P. Pani, *Superradiance: New Frontiers in Black Hole Physics*, *Lect. Notes Phys.* **906** (2015) pp.1 [`1501.06570`].

[19] V. Cardoso, O.J.C. Dias, G.S. Hartnett, M. Middleton, P. Pani and J.E. Santos, *Constraining the mass of dark photons and axion-like particles through black-hole superradiance*, *JCAP* **03** (2018) 043 [`1801.01420`].

[20] M.J. Stott and D.J.E. Marsh, *Black hole spin constraints on the mass spectrum and number of axionlike fields*, *Phys. Rev. D* **98** (2018) 083006 [`1805.02016`].

[21] M.J. Stott, *Ultralight Bosonic Field Mass Bounds from Astrophysical Black Hole Spin*, `2009.07206`.

[22] V.M. Mehta, M. Demirtas, C. Long, D.J.E. Marsh, L. Mcallister and M.J. Stott, *Superradiance Exclusions in the Landscape of Type IIB String Theory*, `2011.08693`.

[23] M. Baryakhtar, M. Galanis, R. Lasenby and O. Simon, *Black hole superradiance of self-interacting scalar fields*, *Phys. Rev. D* **103** (2021) 095019 [`2011.11646`].

[24] D. Blas, D.L. Nacir and S. Sibiryakov, *Ultralight Dark Matter Resonates with Binary Pulsars*, *Phys. Rev. Lett.* **118** (2017) 261102 [`1612.06789`].

[25] D.E. Kaplan, A. Mitridate and T. Trickle, *Constraining fundamental constant variations from ultralight dark matter with pulsar timing arrays*, *Phys. Rev. D* **106** (2022) 035032 [`2205.06817`].

[26] D. Brzeminski, Z. Chacko, A. Dev and A. Hook, *Time-varying fine structure constant from naturally ultralight dark matter*, *Phys. Rev. D* **104** (2021) 075019 [`2012.02787`].

[27] A. Banerjee, G. Perez, M. Safronova, I. Savoray and A. Shalit, *The phenomenology of quadratically coupled ultra light dark matter*, *JHEP* **10** (2023) 042 [`2211.05174`].

[28] T. Damour and J.F. Donoghue, *Phenomenology of the Equivalence Principle with Light Scalars*, *Class. Quant. Grav.* **27** (2010) 202001 [`1007.2790`].

[29] A. Hees, O. Minazzoli, E. Savalle, Y.V. Stadnik and P. Wolf, *Violation of the equivalence principle from light scalar dark matter*, *Phys. Rev. D* **98** (2018) 064051 [`1807.04512`].

[30] A. Hees, O. Minazzoli, E. Savalle, Y.V. Stadnik, P. Wolf and B. Roberts, *Violation of the equivalence principle from light scalar fields: from Dark Matter candidates to scalarized black holes*, in *54th Rencontres de Moriond on Gravitation*, 5, 2019 [`1905.08524`].

[31] Y.V. Stadnik and V.V. Flambaum, *Can dark matter induce cosmological evolution of the fundamental constants of Nature?*, *Phys. Rev. Lett.* **115** (2015) 201301 [`1503.08540`].

[32] Y.V. Stadnik and V.V. Flambaum, *Searching for dark matter and variation of fundamental constants with laser and maser interferometry*, *Phys. Rev. Lett.* **114** (2015) 161301 [`1412.7801`].

[33] Y.V. Stadnik and V.V. Flambaum, *Enhanced effects of variation of the fundamental constants in laser interferometers and application to dark matter detection*, *Phys. Rev. A* **93** (2016) 063630 [`1511.00447`].

[34] Y.V. Stadnik and V.V. Flambaum, *Improved limits on interactions of low-mass spin-0 dark matter from atomic clock spectroscopy*, *Phys. Rev. A* **94** (2016) 022111 [`1605.04028`].

[35] H. Masia-Roig et al., *Intensity interferometry for ultralight bosonic dark matter detection*, *Phys. Rev. D* **108** (2023) 015003 [`2202.02645`].

[36] T. Bouley, P. Sørensen and T.-T. Yu, *Constraints on ultralight scalar dark matter with quadratic couplings*, *JHEP* **03** (2023) 104 [`2211.09826`].

[37] S. Sibiryakov, P. Sørensen and T.-T. Yu, *BBN constraints on universally-coupled ultralight scalar dark matter*, *Journal of High Energy Physics* **2020** (2020) .

[38] I. Akhiezer and S. Peletminskii, *Use of the methods of quantum field theory for the investigation of the thermodynamical properties of a gas of electrons and photons*, *Sov. Phys. JETP* **11** (1960) 1316.

[39] J.I. Kapusta, *Quantum chromodynamics at high temperature*, *Nuclear Physics B* **148** (1979) 461.

[40] M. Quiros, *Finite temperature field theory and phase transitions*, in *ICTP Summer School in High-Energy Physics and Cosmology*, pp. 187–259, 1, 1999 [`hep-ph/9901312`].

[41] J.I. Kapusta and C. Gale, *Finite-temperature field theory: Principles and applications*, Cambridge Monographs on Mathematical Physics, Cambridge University Press (2011), 10.1017/CBO9780511535130.

[42] A.L. Erickcek, N. Barnaby, C. Burrage and Z. Huang, *Chameleons in the Early Universe: Kicks, Rebounds, and Particle Production*, *Phys. Rev. D* **89** (2014) 084074 [`1310.5149`].

[43] V. Mukhanov, *Nucleosynthesis without computer*, *International Journal of Theoretical Physics* **43** (2004) 669.

[44] B.D. Fields and K.A. Olive, *Implications of the non-observation of* ^{6}*Li in halo stars for the primordial* ^{7}*Li problem*, *JCAP* **10** (2022) 078 [`2204.03167`].

[45] Planck collaboration, *Planck 2018 results. VI. Cosmological parameters*, *Astron. Astrophys.* **641** (2020) A6 [`1807.06209`].

[46] A. Coc, N.J. Nunes, K.A. Olive, J.-P. Uzan and E. Vangioni, *Coupled Variations of Fundamental Couplings and Primordial Nucleosynthesis*, *Phys. Rev. D* **76** (2007) 023511 [`astro-ph/0610733`].

[47] T.R. Hemmert, M. Procura and W. Weise, *Quark mass dependence of the nucleon axial vector coupling constant*, *Phys. Rev. D* **68** (2003) 075009 [`hep-lat/0303002`].

[48] J. Kambor and M. Mojzis, *Field redefinitions and wave function renormalization to O(p**4) in heavy baryon chiral perturbation theory*, *JHEP* **04** (1999) 031 [`hep-ph/9901235`].

[49] C.C. Chang et al., *Nucleon axial coupling from Lattice QCD*, *EPJ Web Conf.* **175** (2018) 01008 [`1710.06523`].

[50] A. Walker-Loud et al., *Lattice QCD Determination of* g_A, *PoS* **CD2018** (2020) 020 [`1912.08321`].

[51] C.C. Chang et al., *A per-cent-level determination of the nucleon axial coupling from quantum chromodynamics*, *Nature* **558** (2018) 91 [`1805.12130`].

[52] MICROSCOPE collaboration, *Space test of the Equivalence Principle: first results of the MICROSCOPE mission*, *Class. Quant. Grav.* **36** (2019) 225006 [`1909.10598`].

[53] A. Hees, J. Guéna, M. Abgrall, S. Bize and P. Wolf, *Searching for an oscillating massive scalar field as a dark matter candidate using atomic hyperfine frequency comparisons*, *Phys. Rev. Lett.* **117** (2016) 061301 [`1604.08514`].

[54] H. Davoudiasl and P.B. Denton, *Ultralight Boson Dark Matter and Event Horizon Telescope Observations of M87**, *Phys. Rev. Lett.* **123** (2019) 021102 [`1904.09242`].

[55] L. Badurina, E. Bentine, D. Blas, K. Bongs, D. Bortoletto, T. Bowcock et al., *AION: an atom interferometer observatory and network*, *Journal of Cosmology and Astroparticle Physics* **2020** (2020) 011.

[56] AEDGE collaboration, *AEDGE: Atomic Experiment for Dark Matter and Gravity Exploration in Space*, *EPJ Quant. Technol.* **7** (2020) 6 [`1908.00802`].

[57] D. Antypas et al., *New Horizons: Scalar and Vector Ultralight Dark Matter*, `2203.14915`.

[58] T.A. Wagner, S. Schlamminger, J.H. Gundlach and E.G. Adelberger, *Torsion-balance tests of the weak equivalence principle*, *Class. Quant. Grav.* **29** (2012) 184002 [`1207.2442`].

[59] P. Touboul, G. Metris, V. Lebat and A. Robert, *The MICROSCOPE experiment, ready for the in-orbit test of the equivalence principle*, *Class. Quant. Grav.* **29** (2012) 184010.

[60] MICROSCOPE collaboration, *MICROSCOPE Mission: Final Results of the Test of the Equivalence Principle*, *Phys. Rev. Lett.* **129** (2022) 121102 [`2209.15487`].

[61] A. Derevianko, *Detecting dark-matter waves with a network of precision-measurement tools*, *Phys. Rev. A* **97** (2018) 042506 [`1605.09717`].

[62] K. Van Tilburg, *Wake forces in a background of quadratically coupled mediators*, *Phys. Rev. D* **109** (2024) 096036 [`2401.08745`].

[63] H. Day, D. Liu, M.A. Luty and Y. Zhao, *Blowing in the Dark Matter Wind*, `2312.13345`.

[64] X. Gan, D. Liu, D. Liu, X. Luo and B. Yu, *Detecting Ultralight Dark Matter with Matter Effect*, `2504.11522`.

[65] N. Velez, E. Ritchie, G. Gregory, T. Bouley, D. Wineland, T.-T. Yu et al., *SPUD: SPectroscopy for Ultralight Dark matter*, in *APS Division of Atomic, Molecular and Optical Physics Meeting Abstracts*, vol. 2023 of *APS Meeting Abstracts*, p. F01.130, Jan., 2023.

[66] R. Oswald et al., *Search for Dark-Matter-Induced Oscillations of Fundamental Constants Using Molecular Spectroscopy*, *Phys. Rev. Lett.* **129** (2022) 031302 [`2111.06883`].

[67] D. Budker, J. Eby, M.S. Safronova and O. Tretiak, *Search for fast-oscillating fundamental constants with space missions*, *EPJ Quant. Technol.* **12** (2025) 39 [`2408.10324`].

[68] B.T. Darling and D.M. Dennison, *The water vapor molecule*, *Phys. Rev.* **57** (1940) 128.

[69] J.K. Watson, *Simplification of the molecular vibration-rotation hamiltonian*, *Molecular Physics* **15** (1968) 479 [`https://doi.org/10.1080/00268976800101381`].

[70] J. Wilson, E. Bright and J.B. Howard, *The Vibration-Rotation Energy Levels of Polyatomic Molecules I. Mathematical Theory of Semirigid Asymmetrical Top Molecules*, *The Journal of Chemical Physics* **4** (2004) 260 [`https://pubs.aip.org/aip/jcp/article-pdf/4/4/260/8128068/260_1_online.pdf`].

[71] P. Junnarkar and A. Walker-Loud, *Scalar strange content of the nucleon from lattice QCD*, *Phys. Rev. D* **87** (2013) 114510 [`1301.1114`].

[72] D. Antypas, D. Budker, V.V. Flambaum, M.G. Kozlov, G. Perez and J. Ye, *Fast apparent oscillations of fundamental constants*, *Annalen Phys.* **532** (2020) 1900566 [`1912.01335`].

[73] M.S. Turner, *Periodic signatures for the detection of cosmic axions*, *Phys. Rev. D* **42** (1990) 3572.

[74] C. Zhang et al., *Frequency ratio of the ^{229m}Th nuclear isomeric transition and the ^{87}Sr atomic clock*, *Nature* **633** (2024) 63 [`2406.18719`].

[75] A. Arvanitaki, P.W. Graham, J.M. Hogan, S. Rajendran and K. Van Tilburg, *Search for light scalar dark matter with atomic gravitational wave detectors*, *Phys. Rev. D* **97** (2018) 075020 [`1606.04541`].

[76] A. Laguë, J.R. Bond, R. Hložek, K.K. Rogers, D.J.E. Marsh and D. Grin, *Constraining ultralight axions with galaxy surveys*, *JCAP* **01** (2022) 049 [`2104.07802`].

[77] M. Safarzadeh and D.N. Spergel, *Ultra-light dark matter is incompatible with the milky way's dwarf satellites*, *The Astrophysical Journal* **893** (2020) 21.

[78] DES collaboration, *Milky Way Satellite Census. III. Constraints on Dark Matter Properties from Observations of Milky Way Satellite Galaxies*, *Phys. Rev. Lett.* **126** (2021) 091101 [`2008.00022`].

[79] K. Schutz, *Subhalo mass function and ultralight bosonic dark matter*, *Phys. Rev. D* **101** (2020) 123026 [`2001.05503`].

[80] N. Banik, J. Bovy, G. Bertone, D. Erkal and T.J.L. de Boer, *Novel constraints on the particle nature of dark matter from stellar streams*, *JCAP* **10** (2021) 043 [`1911.02663`].

[81] D.J.E. Marsh and J.C. Niemeyer, *Strong Constraints on Fuzzy Dark Matter from Ultrafaint Dwarf Galaxy Eridanus II*, *Phys. Rev. Lett.* **123** (2019) 051103 [`1810.08543`].

[82] B.T. Chiang, H.-Y. Schive and T. Chiueh, *Soliton Oscillations and Revised Constraints from Eridanus II of Fuzzy Dark Matter*, *Phys. Rev. D* **103** (2021) 103019 [`2104.13359`].

[83] S.A. Teukolsky and W. Press, *Perturbations of a rotating black hole. iii-interaction of the hole with gravitational and electromagnetic radiation*, *The Astrophysical Journal* **193** (1974) 443.

[84] R. Brito, V. Cardoso and P. Pani, *Superradiance*, Springer International Publishing (2020), 10.1007/978-3-030-46622-0.

[85] A. Arvanitaki, S. Dimopoulos, S. Dubovsky, N. Kaloper and J. March-Russell, *String Axiverse*, *Phys. Rev. D* **81** (2010) 123530 [`0905.4720`].

[86] A. Arvanitaki, M. Baryakhtar and X. Huang, *Discovering the QCD Axion with Black Holes and Gravitational Waves*, *Phys. Rev. D* **91** (2015) 084011 [`1411.2263`].

[87] C. Ünal, F. Pacucci and A. Loeb, *Properties of ultralight bosons from heavy quasar spins via superradiance*, *JCAP* **05** (2021) 007 [`2012.12790`].

[88] P. Du, D. Egana-Ugrinovic, R. Essig, G. Fragione and R. Perna, *Searching for ultra-light bosons and constraining black hole spin distributions with stellar tidal disruption events*, *Nature Commun.* **13** (2022) 4626 [`2202.01215`].

[89] H. Fukuda and K. Nakayama, *Aspects of Nonlinear Effect on Black Hole Superradiance*, *JHEP* **01** (2020) 128 [`1910.06308`].

[90] A. Mathur, S. Rajendran and E.H. Tanin, *Clockwork mechanism to remove superradiance limits*, *Phys. Rev. D* **102** (2020) 055015 [`2004.12326`].